ATOMISTIC MODELING OF GRAPHENE NANOSTRUCTURES AND SINGLE-ELECTRON QUANTUM DOTS

A Thesis

Submitted to the Faculty

of

Purdue University

by

Junzhe Geng

In Partial Fulfillment of the

Requirements for the Degree

of

Master of Science in Electrical and Computer Engineering

August 2012

Purdue University

West Lafayette, Indiana

To my parents

ACKNOWLEDGMENTS

As I finish another chapter of my life, I would like to take this opportunity to thank a number of people who have influenced my life.

First of all, I would like to thank professor Gerhard Klimeck, without whom this work would not be possible. I feel very fortunate to have the opportunity to work and learn in his research group. During the past two years, I have learned many valuable lessons from him, such as how to conduct independent research, how to present my work and articulate my ideas. These lessons will have a lasting impact both in my career and in my life.

I would also like to thank professor Mark Lundstrom and Timothy Fisher for being my committee members, examining my work and giving me their valuable opinions. Professor Lundstrom's course 'Electronic Transport in Semiconductors (ECE 656)' and professor Supriyo Datta's course 'Quantum Transport: Atom to Transistor (ECE 659)' have provided me the essential knowledge and insight on device modeling and research.

I would like to express my gratitude to Sunhee Lee and Hoon Ryu for being my mentors and patiently guiding me with the quantum dot work. They have shown me what it takes to be successful in graduate school, by setting excellent examples themselves. Their experiences are truly inspirational and I wish them nothing but the best in their respective new careers.

I would like to thank Tillmann Kubis, SungGeun Kim, Jim Fonseca, who have provided me help in graphene modeling work. I enjoyed working with them all.

I would like to acknowledge the NEMO5 team, especially Michael Povolotskyi and Yu He, for providing software support for the modeling work of graphene nanostructures.

I would also like to thank professor Zhihong Chen, and her PhD student Tao Chu, for helpful discussions on graphene nanomeshes.

I am grateful to Yaohua Tan and Yu He, from whom I have obtained a lot of help through discussions. I also appreciate them as my awesome roommates. I appreciate Xufeng Wang and Matthias (Yui-Hong) Tan for helping me in various occasions, such as revising this thesis. I also want to thank some friends and colleagues Zhengping Jiang, Lang Zeng, Kai Miao, Yuling Hsueh, Abhijeet Paul, Mehdi Salmani, Parijat Sengupta, Ganesh Hegde for making the past two years in the lab a worthy experience for me.

A special thanks goes to the Purdue Crew team. Collegiate rowing in my first year was a memorable experience, which taught me the importance of teamwork, perseverance and fortitude in sports and life.

Last but not least, I would like to give my sincerest thanks to my parents, my family, and my girlfriend Yu-Tung Hou, for their selfless love and support. They are the biggest motivation in my life.

TABLE OF CONTENTS

Page

LIST OF FIGURES

Figure Page

ABBREVIATIONS

MOS	Metal-Oxide-Semiconductor
QD	Quantum Dot
VS	Valley-Splitting
DIBL	Drain-Induced Barrier Lowering
SS	Sub-Threshold Swing
GNM	Graphene Nano-Mesh
GNR	Graphene Nano-Ribbon
AGNR	Armchair Graphene Nano-Ribbon
ZGNR	Zigzag Graphene Nano-Ribbon
AGNM	Armchair Graphene Nano-Mesh
ZGNM	Zigzag Graphene Nano-Mesh
Si:P	Densely Phosphorous Doped Silicon
NEGF	Non-Equilibrium Green's Function
NEMO5	Fifth Edition of the NanoElectronics MOdeling Tools

ABSTRACT

Geng, Junzhe. M.S.E.C.E., Purdue University, August 2012. Atomistic Modeling of Graphene Nanostructures and Single-Electron Quantum Dots. Major Professor: Gerhard Klimeck.

The technological advancement in the semiconductor industry in the past few decades has mainly been driven by the continuous down-scaling of CMOS devices following Moore's Law [1]. However, device scaling is fundamentally limited by a number of technological issues, such as short-channel effects. The length scale of today's device is quickly approaching its fundamental limit [3]. As a result, extensive research efforts are invested to find new materials and novel device concepts to enhance device performance. Computational modeling serves as a highly effective and efficient approach in exploring these materials and device concepts. This work utilizes several computational modeling methods to study two types of devices (a) graphene based nanostructures, and (b) silicon based quantum dots.

The first part of this thesis is focused on modeling a new class of graphene based nanostructures, namely graphene nanomesh (GNM). It is a 2D nanostructure obtained by fabricating periodic perforations on a piece of graphene sheet. According to experimental studies [18] [19], this is an effective approach of tuning the bandgap. This work applies an advanced nearest-neighbor tight-binding model [20] in the electronic structure calculation of GNM. The model details as well as its advantages compared to the conventional model are discussed. Transport properties of GNM are investigated using non-equilibrium Green's function (NEGF) method. Two types of hole geometries in GNM, circular and rectangular holes, are studied in details. It is demonstrated that bandstructures of GNM can be engineered via hole geometry. Some intriguing features in the GNM bandstructures are observed, such as

dispersionless bands, edge localization of electron wavefunctions, anisotropic dispersion relations. The effects of edge geometries (zigzag vs. armchair) in GNM on its electronic structure and transport properties are investigated. Lastly, some novel device applications that utilize these unique electronic properties of GNM are proposed.

The second half of this work is focused on predicting valley splitting (VS) in an electrostatically defined silicon quantum dot. The significance of VS for quantum information storage is explained. Eigenstates of the quantum dot have been calculated charge self-consistently and the VS has been extracted under various biasing conditions. Simulation results indicate that the VS in this quantum dot can be controlled by tuning the potential barrier and gate geometry. Full range of the achievable VS is determined. This information is vital in guiding the design of Si quantum dots with desired VS.

1. INTRODUCTION

1.1 The Device Scaling Challenge

In the past few decades, the semiconductor industry has seen steady and rapid development as the technology node scaling down following Moore's Law [1]. For decades, making MOSFETs smaller has been key to the progress in the digital logic. The down-scaling of transistor size has enabled increasing complexity of integrated circuits as more transistors are able to fit into a single chip. Such a phenomenon was best summarized by Moore's Law, which states that the number of transistors in a single integrated circuit doubles every 18 months [1] [2]. As a result, we have witnessed dramatic advances in electronics that have found uses in computing, communications, and other applications that affect just about every aspect of our lives.

However, performance enhancement of devices through scaling cannot continue forever. The continuing scaling of CMOS transistors is heavily hampered due to a number of technological limits, among which the most prominent is the short channel effect (SCE), which is the major source of device degradation as the MOSFET channel length scales down. One of the most outstanding SCE is the drain induced barrier lowering(DIBL, Fig. 1.1), in which the effect of drain terminal lowers the potential barrier seen by the electrons in the source, thus making the electrons easier to climb over the barrier. The result of DIBL is undesirable, large off-state leakage current. Therefore, DIBL is highly undesirable and detrimental to device operation because it not only makes the device harder to be turned off, but also induces large power leakage at the off-state. DIBL is more severe for short channel length devices. The practical consideration on power leakage limits the physical length of a planer CMOS device to $\sim$10 nm [3].

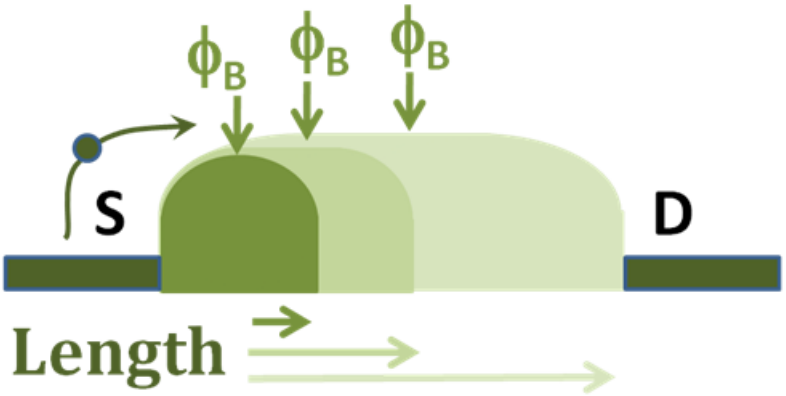

Fig. 1.1. Illustration of potential barrier lowering of MOSFET. As channel length decreases, the barrier ϕ_B to be surmounted by an electron from the source on its way to the drain reduces. (Image from Wikipedia [53])

Fig. 1.2 shows the evolution of MOSFET gate length in production-stage integrated circuits as well as the number of transistors in a single processor chip. As shown, the length of today's MOSFET has already scaled down to tens of nanomenters, which is quickly approaching the planner CMOS limit. There is growing concern in the semiconductor industry that MOSFET scaling is approaching its limits and that, in the long run, it will be necessary to introduce new material and device concepts to ensure that performance continues to improve. Such concern has lead to research towards potential new transistor channel materials such as Ge, InAs, graphene and new device structures such as finFET, gate-all-around FET and band-to-band tunnelling (BTBT) transistors. Innovative concepts like quantum computing, which utilizes the electron's spin information as a quantum information unit (qubit), has also been proposed [26] and drawn tremendous amount of attention and excitement.

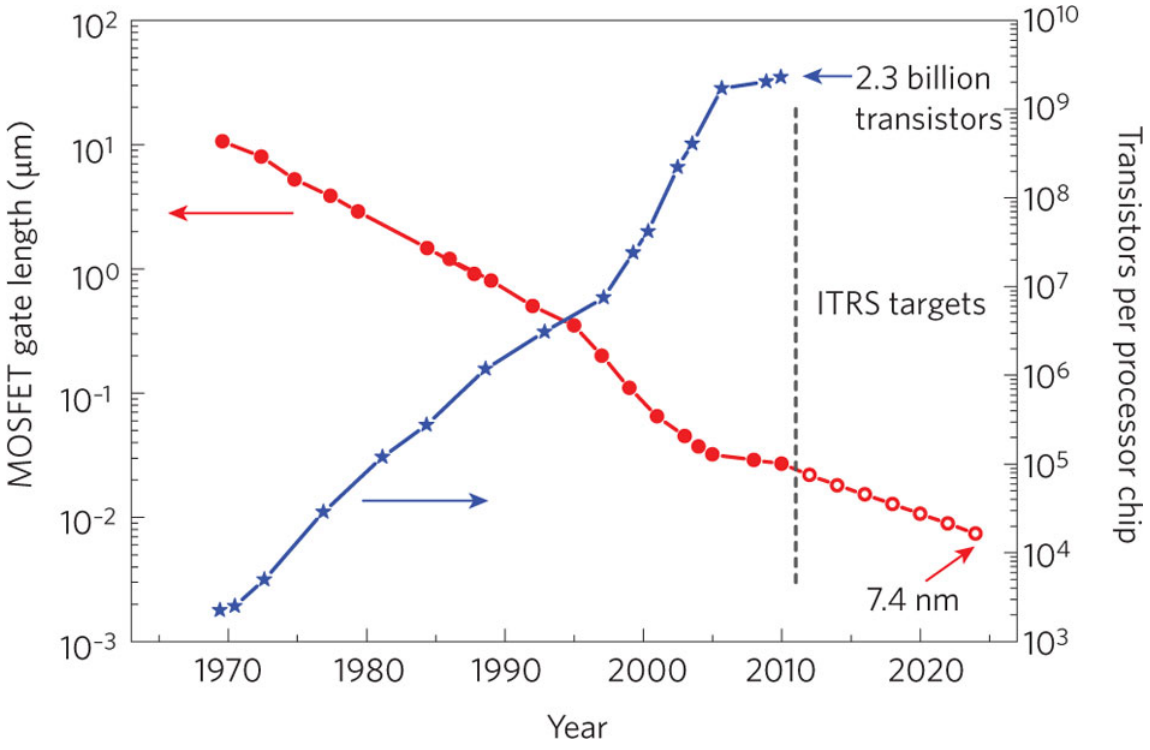

Fig. 1.2. Evolution of MOSFET gate length in production-stage integrated circuits(filled red circles) and International Technology Roadmap for Semiconductors (ITRS) targets (open red circles). As gate length being reduced, the number of transistors per processor chip has increased (blue stars). Maintaining these trends is a significant challenge for the semiconductor industry, which is why new materials and new device structures are being investigated. [3]

1.2 The Role of Computational Modeling

When it comes to utilizing nano-scale device concepts to target the current technological issues, the possibilities are endless. Such is mainly because of the complexity and many aspects of electronic device structures, such as dimension, orientation, gate/channel materials. However, a large portion of these concepts do not see their applications in real devices. Because the fabrication of integrated circuits is a highly complicated art, semiconductor fabrication plants are extremely expensive (several billions of US dollars [3]). It is highly costly for the semiconductor industry to mas-

sively produce a new device based on fundamentally different structures and physics other than CMOS, or a different material other than Si. Therefore, for a new device structure or material to be of any practical use for industry, it must be fabricated and tested repeatedly in laboratories. However, even the experimental approach to device engineering can be very expensive which cannot afford to experiment with the numerous aspects of device via 'trial and error'. Computational modeling serves such purpose and covers the limitation of the experimental approach. Computational modeling approaches utilize established device theory and electronic models, to simulate and test various aspects of device engineering, taking advantage of efficient computational methods and abundant computing resources. Computational modeling not only serves for theoretical studies but also for developing guidelines for experimental design and testing of novel electronic devices.

1.3 Need for Atomistic Modeling and Quantum Transport

Today's device length scale has already reached sub-micron regime (figure 1.2), and device size will reach below 10 nm in the very near future. At such small length-scale, the device characteristics are heavily influenced by quantum mechanical effects and the exact bandstructure of device. Therefore, atomistic approaches are necessary in order to model these nanoscale devices and reveal their physics. For example, when it comes to carrier transport in nanoscale devices, semi-classical methods such as drift-diffusion equation do not describe the carrier behavior well. Quantum transport methods such as the non-equilibrium green's function (NEGF) method must be utilized to correctly take the quantum mechanical behaviors into account.

1.4 Outline of This Thesis

This thesis applies computational modeling to explore (1) Graphene based nanostructures and (2) Si based single-electron quantum dots. Both of these two subjects are studied utilizing atomistic modeling (and) quantum transport approaches. Chap-

ter 2 will discuss the graphene nanostructure, which has drawn a lot of excitement due to its potential of replacing Si as the channel material for next generation devices. Chapter 3 will focus on Si single-electron quantum dots, which have been proposed as a design candidate for spin qubits. Chapter 4 will summarize the work in this thesis and present a proposal for future work.

2. ATOMISTIC MODELING OF GRAPHENE NANOMESHES

2.1 Introduction: Emergence of Graphene Devices

Graphene is a single 2D sheet of carbon atoms arranged in a honeycomb lattice as shown in Fig. 2.1. Its electronics properties was first studied by P.R Wallace in 1947 [6]. However, its rise to stardom only started in recent years. In October 2004, physicists reported that they had prepared graphene and observed the electric field effect in their samples [4]. Since then, graphene has attracted enormous interest not only among physicists and material scientists, but also in the electronic device community, which has been actively seeking for new materials to potentially replace Si in next generation devices in order to continue the device scaling trend. Graphene possesses a number of extraordinary characteristics that makes it such an attractive material for future electronic devices.

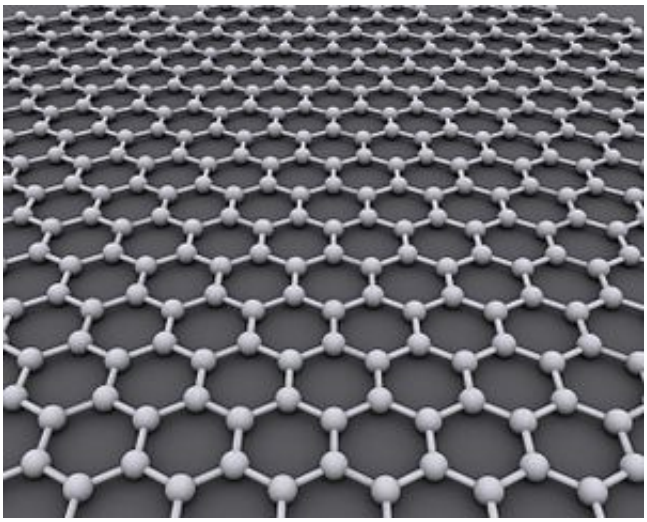

Fig. 2.1. Graphene 2D lattice, showing the honeycomb arrangement of carbon atoms (Image from Wikipedia [52])

2.1.1 Advantages of Graphene

High Mobility

One of the most outstanding properties of graphene is its high electron mobility, which is a key property in defining a good device channel material because mobility is strongly related to carrier transport characteristics and device performance. Mobilities of 10^6 $cm^2V^{-1}s^{-1}$ have been reported for suspended graphene [12], which is many orders of magnitude higher than conventional semiconductor materials like Si.

Good High-Field Transport

However, mobility only describes carrier transport well in the low-field regime. As the gate length of modern FET scales down, a significant portion of device channel is in the high-field regime, where electron velocity is the deciding factor of carrier transport characteristics. Therefore, a deeper look into the electron velocity in graphene, especially under high electrical field, is necessary in order to determine the electron

transport performance in graphene. Fig. 2.2 compares the electron drift velocity of graphene, carbon nanotubes, and common semiconductors such as Si, GaAs,and $In_{0.53}Ga_{0.47}As$ under various electric fields. The curves clearly show that graphene and carbon nanotubes have much higher electron velocity than the common semiconductors at under all range of E-fields. Furthermore, the decrease of electron velocity at higher E-fields is much slower in graphene than in common semiconductors. Therefore, regarding high-field transport, graphene has a clear advantage over conventional semiconductors. Such advantage can potentially result in graphene finding application in high-frequency device, where rapid response of electron is required.

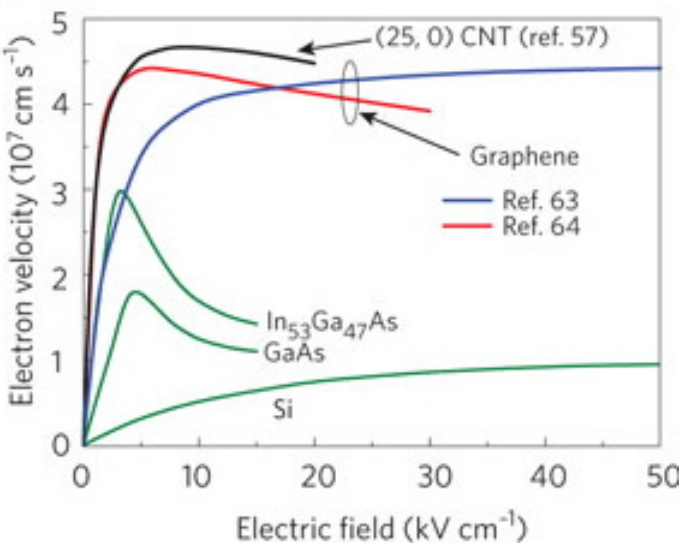

Fig. 2.2. Electron drift velocity versus electric field for common semiconductors (Si, GaAs, $In_{0.53}Ga_{0.47}As$), a carbon nanotube and large-area graphene (ref. [7])

Low Dimensionality

Another big, if not the biggest advantage of graphene as a FET channel material is that it is a two-dimensional material. Graphene based FET has the potential of having single-atomic layer thickness, which is the ultimate device scaling limit. With

a thin channel, graphene FET will be robust against short-channel effects down to very short gate lengths [13], thus having superior gate controllability.

2.1.2 Challenge of Graphene Devices: Bandgap Opening

Despite all the attractive properties of graphene, there is one major drawback that hinders graphene's major breakthrough in real device applications — it has zero bandgap! As can be seen from the graphene bandstructure in Fig. 2.3, the conduction and valence bands of graphene are cone shaped at K points and their tips connect, which leads to the zero bandgap. As a result, large area graphene sheet cannot be directly used in digital logic devices since it does not have an "off" state due to zero bandgap.

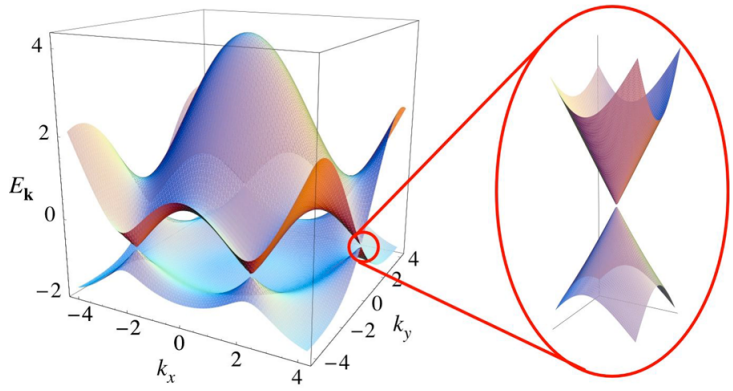

Fig. 2.3. Graphene bandstructure. Conduction and valence bands are cone-shaped and meet at K points, resulting in zero bandgap (zoomed in). Image taken from [14]

Extensive research efforts, both theoretical and experimental have been devoted in finding methods to open up a band gap in graphene (Fig. 2.4). Such methods include constraining large-area graphene in one dimension to form graphene nanoribbons [8], biasing bilayer graphene [9], epitaxial growth of graphene on SiC [10] and applying strain to graphene [11].

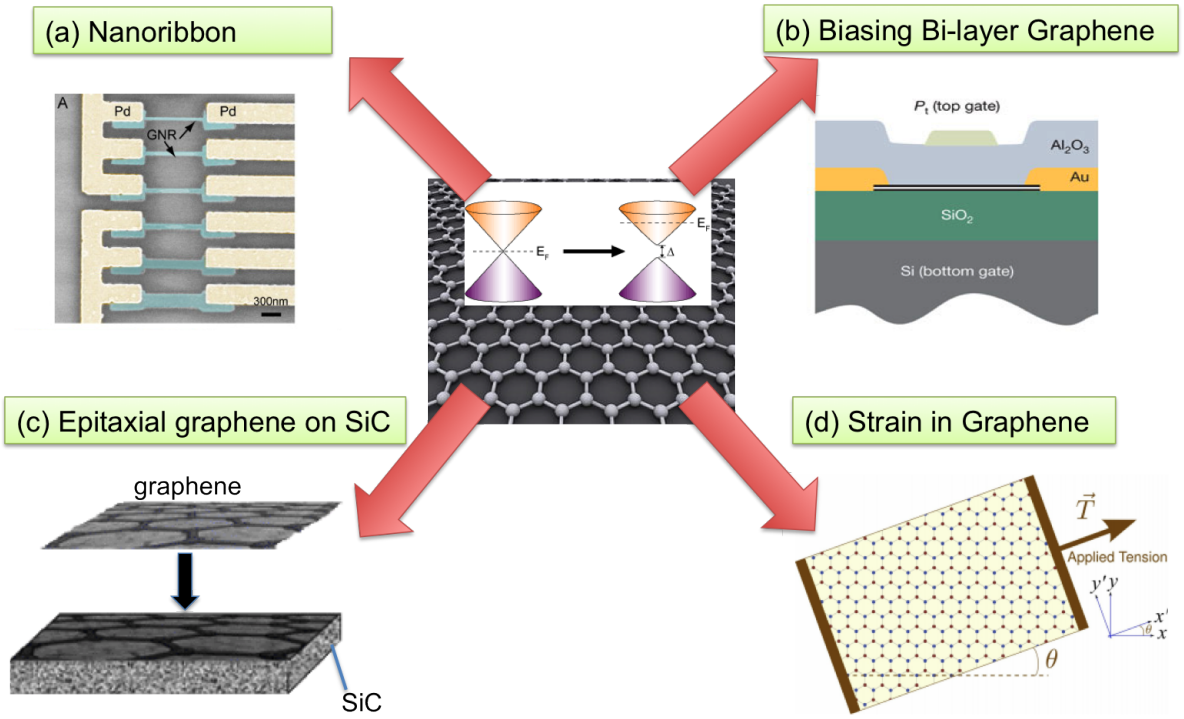

Fig. 2.4. Various bandgap opening techniques in graphene. (a) Graphene nanoribbons [8]. (b) Biasing by-layer graphene [9]. (c) Epitaxial growth of graphene on SiC [10]. (d) Applying strain in graphene [11].

Graphene Nanoribbon

Among the various bandgap-opening approaches, the graphene nanoribbon(GNR) method is among the most popular. It has been predicted GNRs with width less than 10 nm have a bandgap that is inversely proportional to the width of the nanoribbon [15]. The opening of a bandgap in nanoribbons has been verified experimentally [16].

However, in order to open a bandgap useful for conventional field-effect devices, very narrow nanoribbons with well-defined edges are needed. This is because the electronic properties of graphene nanoribbon are very sensitive to edge roughness and ribbon width fluctuations [17]. This presents a great challenge in GNR fabrication processes because it is very difficult to achieve GNR with clean edges. Moreover, nanoribbon devices often have low driving currents or transconductances. Practical

devices and circuits will require the production of dense arrays of ordered nanoribbons, which poses additional challenges in the fabrication process.

Graphene Nanomesh

Recently, experimentalists have successfully fabricated a new graphene nanostructure — graphene nanomesh(GNM) [18], which can open up a bandgap in a large sheet of graphene. Graphene nanomeshes are prepared using block copolymer lithography to punch periodic pores in a graphene sheet. The fabrication process is shown in Fig. 2.5. The hole periodicity as well as neckwidth can be varied, and as a result, various sizes of bandgaps can be obtained. It was also reported by Bai et al. [18] that a GNM FET can support current that is nearly 100 times larger than in individual GNR devices, while maintaining a similar on-off ratio. The bandgap and on-off ratio can also be tuned by varying the neckwidth.

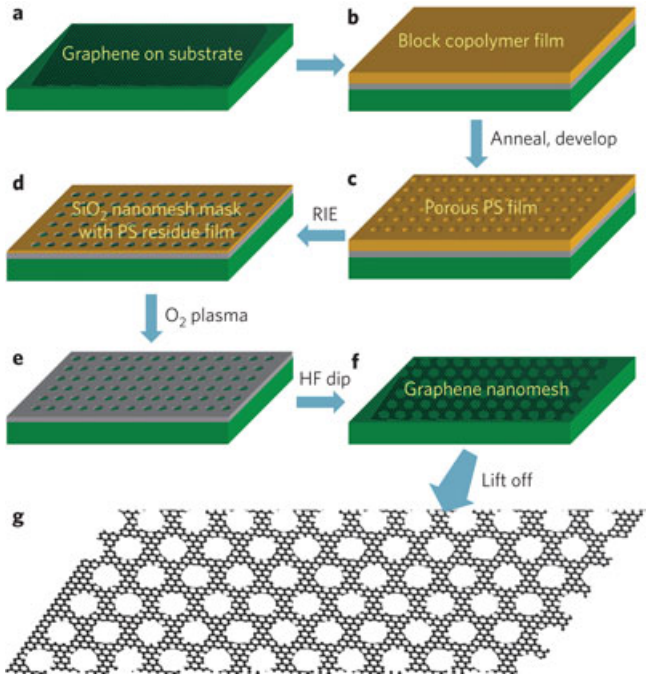

Fig. 2.5. Schematic of fabrication of a graphene nanomesh using block copolymer lithography (ref [18])

2.1.3 Objectives of This Work

The goal of this work is to explore the potential of GNM based devices by conducting an elaborative simulation study on various GNM structures. By investigating the electronic and transport properties of GNM, we hope to find answers to the following questions:

- What factor determines the bandgap in GNM?
- How does the edge geometry affect both the electronic and transport properties?
- What, if any, are the potential applications for GNM devices?

This chapter is organized as follows. The next section covers information about the model and approach used to study GNM. Subsequently results are presented and explained, and lastly, based on the results, some potential application ideas are put forward.

2.2 Methodology

2.2.1 Electronic Model: The Tight-Binding Approach

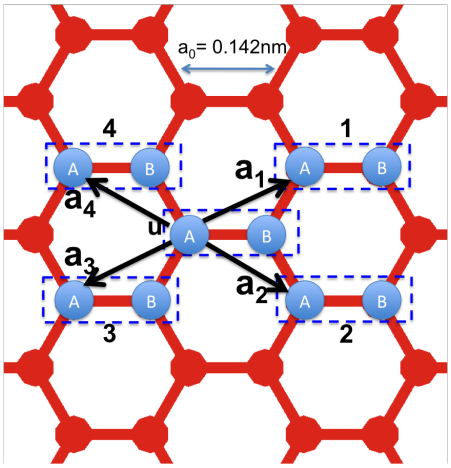

Fig. 2.6. Arrangement of carbon atoms on graphene, showing the unitcell structure. The lattice constant is a_0=0.142 nm. The graphene lattice is formed by translating the unitcell(marked by blue boxes) periodically in 2D with respect to basis vectors $\vec{a_1}$ and $\vec{a_2}$. Each unitcell contains two carbon atoms A and B, and it has four nearest neighbors 1-4.

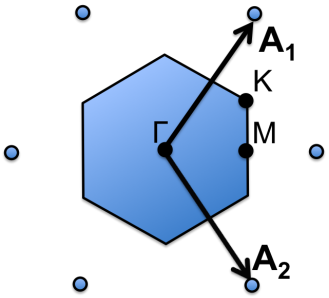

Fig. 2.7. Reciprocal lattice with basis vector $\vec{A_1}$ and $\vec{A_2}$ such that $\vec{A_1} \cdot \vec{a_1} = \vec{A_2} \cdot \vec{a_2} = 2\pi$ and $\vec{A_1} \cdot \vec{a_2} = \vec{A_2} \cdot \vec{a_1} = 0$. The Brillouin zone is the shaded blue region obtained by drawing the perpendicular bisectors of the lines joining the Γ point to the six neighboring points on the reciprocal lattices.

Fig. 2.6 shows the arrangement of atoms in the graphene lattice. The graphene lattice is two-dimensional and consists of six carbon atoms arranged in a hexagonal shape. The distance between two neighboring carbon atoms is 0.142 nm, which is the lattice constant a_0. A single graphene unitcell contains two carbon atoms A and B (shown as a blue box in fig 2.6), and the atoms are grouped so that any two unitcells have exactly same surrounding. The graphene lattice can be formed by repeating a unitcell periodically in 2D. Fig. 2.6 shows a unitcell 'u' in the center and its four neighboring unitcells, marked as 1-4. The basis vectors by which the lattice is formed are $\vec{a_1}$ and $\vec{a_2}$, which are the vectors connecting 'u' from its neighbor '1' and '2':

$$\vec{a_1} = \frac{3a_0}{2}\hat{x} + \frac{\sqrt{3}a_0}{2}\hat{y} \tag{2.1}$$

$$\vec{a_2} = \frac{3a_0}{2}\hat{x} - \frac{\sqrt{3}a_0}{2}\hat{y} \tag{2.2}$$

and the vectors to the other two unitcells 3 and 4 can be obtained from $\vec{a_1}$ and $\vec{a_2}$ by:

$$\vec{a_3} = -\vec{a_1} \tag{2.3}$$

$$\vec{a_4} = -\vec{a_2} \tag{2.4}$$

The reciprocal lattice are formed with vectors $\vec{A_1}$ and $\vec{A_2}$, which can be constructed from relation:

$$\vec{A_j} \cdot \vec{a_i} = 2\pi\delta_{ij} \tag{2.5}$$

for graphene, the relation simplifies to:

$$\vec{A_1} \cdot \vec{a_1} = \vec{A_2} \cdot \vec{a_2} = 2\pi; \vec{A_1} \cdot \vec{a_2} = \vec{A_2} \cdot \vec{a_1} = 0 \tag{2.6}$$

and combined with 2.1 2.2, $\vec{A_1}, \vec{A_2}$ can be obtained as:

$$\vec{A_1} = \frac{2\pi}{3a_0}\vec{x} + \frac{2\pi}{\sqrt{3}a_0}\vec{y} \tag{2.7}$$

$$\vec{A_2} = \frac{2\pi}{3a_0}\vec{x} - \frac{2\pi}{\sqrt{3}a_0}\vec{y} \tag{2.8}$$

Fig. 2.7 shows the reciprocal lattice constructed from basis $\vec{A_1}$ and $\vec{A_2}$. The Brillouin zone (shaded blue region) is obtained by drawing the perpendicular bisectors of the lines joining the origin [0,0] to the six neighboring points on the reciprocal lattices. Also marked on the reciprocal lattice are important symmetry points Γ, which is the center of the Brillouin zone, K which are the corners of the Brillouin zone, and M, which are the mid-points of Brillouin zone edges.

In order to obtain the bandstructure, the matrix form of Schrodinger equation with nearest-neighbor approximation:

$$\sum_m [H_{nm}]\phi_m = E\phi_n \tag{2.9}$$

must be solved, where n is the index of the unitcell and m is the index of its nearest neighbors. H_{nm} is the coupling matrix from unitcell n to m, which has dimension (b x b), where b is the number of atoms per unitcell multiplied by the number of basis (explained later) in each atom. ϕ_m is a (b×1) column vector denoting the wavefunction in unit cell m, and it follows the Bloch's theorem:

$$\phi_m = \phi_0 e^{i\vec{k}\cdot\vec{d_m}} \tag{2.10}$$

The matrix equation in (2.9) can then be simplified using (2.10) to:

$$E\phi_0 = [h(\vec{k})]\phi_0 \tag{2.11}$$

where

$$[h(\vec{k})] = \sum [H_{nm}] e^{i\vec{k}\cdot(\vec{d_m}-\vec{d_n})} \tag{2.12}$$

is the Hamiltonian matrix. The bandstructure is obtained by finding the eigenvalues of the Hamiltonian, which is a (b×b) matrix. For graphene, each carbon atom has four valence orbitals (2s, $2p_x$, $2p_y$, $2p_z$), however, the electronic structure of graphene can be described quite well using only the $2p_z$ orbital. This is because the energy levels involving 2s, $2p_x$, $2p_y$ orbitals are largely decoupled from those involving $2p_z$

orbitals [6]. More importantly, energy levels yielded by $2p_z$ orbitals are close to the Fermi level, where electron conduction happens. Such a one band tight-binding model for graphene, where only the $2p_z$ orbital is used is known as the 'pz model'. Using the pz model, the Hamiltonian matrix in (2.12) becomes a (2×2) matrix since there are two atoms in each unit cell and one basis representing each atom.

If we assume the onsite element to be zero for convenience, and coupling between neighboring carbon atoms to be -t, then the coupling matrices can be written as:

$$[H_{uu}] = \begin{bmatrix} 0 & -t \\ -t & 0 \end{bmatrix}$$

$$[H_{u1}] = [H_{u2}] = \begin{bmatrix} 0 & 0 \\ -t & 0 \end{bmatrix}$$

$$[H_{u3}] = [H_{u4}] = \begin{bmatrix} 0 & -t \\ 0 & 0 \end{bmatrix}$$

The Hamiltonian can be constructed according to equation 2.12:

$$[h(\vec{k})] = [H_{uu}] + [H_{u1}]e^{i\vec{k}\cdot\vec{a_1}} + [H_{u2}]e^{i\vec{k}\cdot\vec{a_2}} + [H_{u3}]e^{i\vec{k}\cdot\vec{a_3}} + [H_{u4}]e^{i\vec{k}\cdot\vec{a_4}} \tag{2.13}$$

substituting in eq.2.1-2.4 and the coupling matrices, equation 2.13 becomes:

$$h[\vec{k}] = \begin{bmatrix} 0 & -t(1 + e^{i\vec{k}\cdot\vec{a_1}} + e^{i\vec{k}\cdot\vec{a_2}}) \\ -t(1 + e^{-i\vec{k}\cdot\vec{a_1}} + e^{-i\vec{k}\cdot\vec{a_2}}) & 0 \end{bmatrix}$$

replacing $\vec{k}$ with $k_x\hat{x} + k_y\hat{y}$, and $\vec{a}$ with $a_x\hat{x} + a_y\hat{y}$, simplify, and the analytical form of E-k relation is obtained:

$$E = \pm\sqrt{1 + 4cos(\frac{2\pi}{\sqrt{3}a_0}k_y)cos(\frac{2\pi}{3a_0}k_x) + 4cos^2(\frac{2\pi}{\sqrt{3}a_0}k_y)} \tag{2.14}$$

2.2.2 Band Model of Graphene: P/D Model

The pz model described in the previous section is a widely popular method of representing the graphene electronic structure. It is simple and computationally efficient,

and it describes general features of the graphene bandstructure well. However, it does not include enough physics in order to accurately represent the electronic structure of graphene and its nanostructures, such as GNR. There are mainly two issues with the pz model. First, it does not correctly reproduce the asymmetry of the graphene bandstructure at M, which is present in the *ab initio* calculations. Fig. 2.8 compares bulk graphene bandstructure calculated from *ab initio* method (DFT+GW) and pz model, The DFT+GW calculation produces an asymmetric bandstructure around the M point, while the pz model produces exact symmetry at the M point. The difference at the M points for these two different methods is around 0.8 eV. Secondly, the single-pz model does not allow hydrogen passivation on graphene edges. Because hydrogen atoms modeled by a single s-orbital has no coupling to the π-bands. Such shortcoming has resulted in incorrect bandgap calculation for AGNR [20].

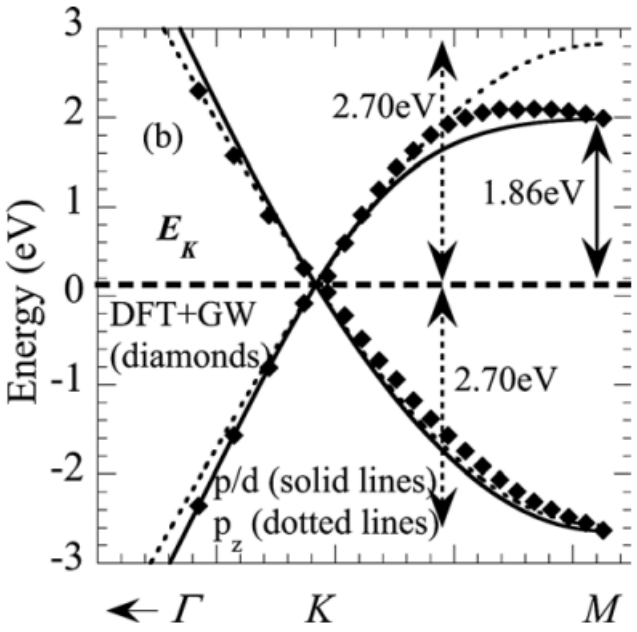

Fig. 2.8. Bulk graphene bandstructure in the vicinity of K calculated using three different methods: DFT+GW(diamonds), the p/d model (solid lines), and the pz model (dotted lines). The DFT+GW calculation produces asymmetric bandstructure around the M point, while the pz model produces exact symmetry at M point. The p/d model is able reproduce such asymmetry quite well. Image taken from ref. [20]

Boykin et al. [20] provided a solution to the above problem by coming up with a new tight-binding model for graphene. It is a nearest neighbor tight-binding model that includes not only the p_z orbital, but also two of the 3d orbitals: d_{yz} and d_{zx}. Together they form a three-orbital orthogonal basis $\{p_z, d_{yz}, d_{zx}\}$.

In order to include proper hydrogen passivation, the same basis set $\{p_z, d_{yz}, d_{zx}\}$ is provided for the hydrogen atoms as well. The parameters are obtained from fitting from DFT calculations [20]. Including the three-basis set in H atoms induces coupling between orbitals in H atoms and orbitals in C atoms. Thus, the p/d model allows hydrogen passivation to be included explicitly in the tight-binding Hamiltonian.

The p/d model is able to correctly reproduce the asymmetry of the E-k relation around the M point, as can been seen from fig 2.8. This is because the bands resulted

from higher energy d orbitals have different coupling effects to the two π bands, resulting in asymmetric π bands above and below the Dirac point. Furthermore, the bandstructure produced by the p/d model with hydrogen passivation for AGNRs shows better agreement with DFT calculations [20].

2.2.3 Validation of P/D Model

Since the p/d model has included essential physics of bulk graphene and hydrogen passivation, it is utilized in this work to study the electronic properties of GNM. However, before starting any modeling tasks of graphene structures, it is necessary to verify the band model that is being used.

Bandstructure Comparison for Graphene

As previously described, one of the major problems of the pz model is that it does not correctly capture the band asymmetry around the M point. The bandstructure of graphene calculated using the p/d model should be able to reveal such asymmetry. Therefore, the first test of the model is to compare the bandstructure of graphene calculated from the two different band models.

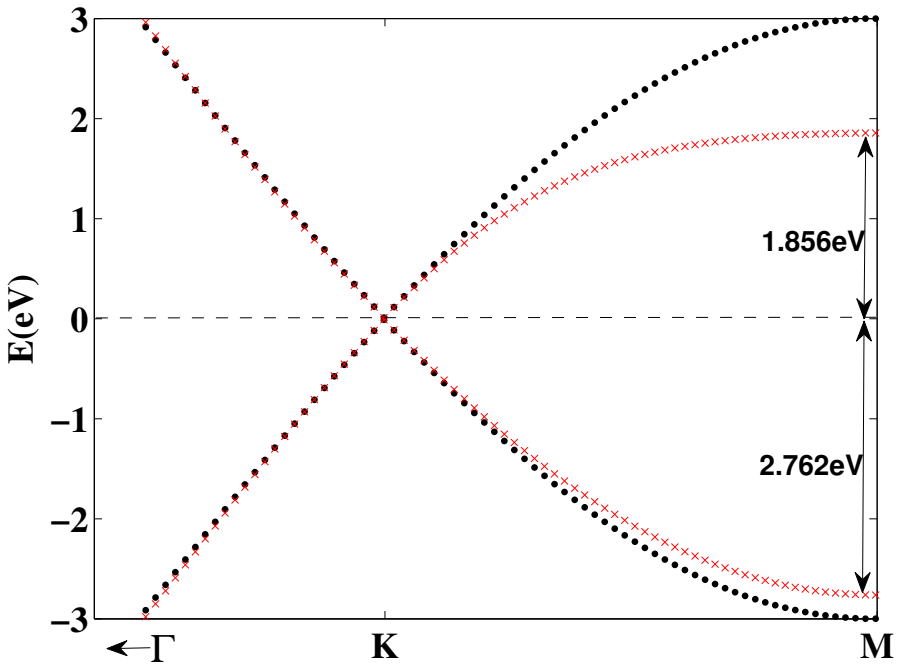

Fig. 2.9. Calculation of bulk graphene bandstructure using pz(black dot) and p/d model(red cross). As shown, the pz model produces bands symmetric along the Dirac point(E=0), while p/d calculation produces bands asymmetric, just as expected from [20]

As can be seen from Fig. 2.9, the bandstructure calculated using the p/d model(red cross) is indeed asymmetric around the Dirac point. At the M point, the energy state from the lower band is at -2.76 eV, while the state from the upper band is at 1.86 eV. In comparison, the two states at the M point from the pz bandstructure is located at around -3 eV and 3 eV. This calculation is a strong indication that the p/d model for graphene has been correctly implemented.

A Sanity Check: 10-ZGNR

For the second test, a 10 atomic layers wide zigzag graphene nanoribbon (10-ZGNR) was constructred, Fig. 2.10 displays the (a) bandstructure (b) transmission

calculated using the two different models pz and p/d. Bandstructure calculated using both models reveal the metallic nature of zigzag GNR, as shown, the conduction and valence bands meet each other at E = 0 eV, yielding zero bandgap. However, the p/d result also reveals the band bending at the tail ends of the bandstructure (marked with green circles), where the pz result indicates completely flat bands. As a result, the transmission T(E) result from p/d calculation has a 'spike' at around E = 0 eV, i.e, T(E=0) = 3. Such a spike in the transmission is also observed in various other DFT calculations [24] [23]. Such excellent agreement of our tight-binding results with DFT calculations is another proof that the p/d model includes the essential physics to describe the properties of graphene nanostructures.

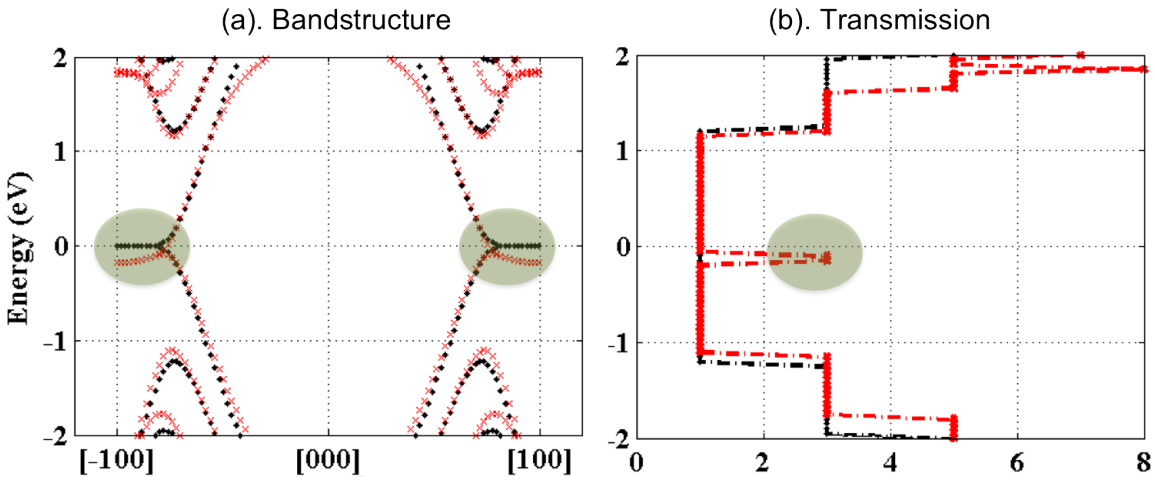

Fig. 2.10. (a) Bandstructure (b) Transmission calculated with pz (black) and p/d (red) models for a 10-ZGNR. The biggest difference is around Dirac points where the conduction bands and valence bands meet. For p/d calculation, the bands around Dirac is not perfectly flat, as compared to the pz calculation, which leads to a spike in the transmission of T(E) = 3.

With the above two test, it is convincible that we have a decent electronic model in p/d model that contains the essential physics of carbon atoms in graphene. We will utilize the p/d model in our simulation study of graphene nanomesh.

Simulation study of GNM in this chapter is carried out with NEMO 5, the fifth edition of the nanoelectronics modeling Tools of the Klimeck group. The core capabilities of NEMO5 lie in the atomic-resolution calculation of nanostructure properties using the tight-binding model, self-consistent Schroedinger-Poisson calculations, and quantum transport [5].

2.3 Results For Graphene Nanomeshes

2.3.1 Circular Hole Structures: Bandgap Engineering

The first topic for GNM study is the most sought-after property, namely the bandgap. The ability of GNM to open bandgaps by tuning its neckwidth makes it an attractive material for electronic devices. There have been experimental efforts in fabricating GNMs with varying neckwidths and measuring the bandgap. Liang et al. [19] have fabricated graphene nanomeshes where pores are arranged in hexagonal shapes and are separated by less than 10 nm, as shown in Fig. 2.11. They also measured the bandgap versus neckwidth, which is shown in Fig. 2.12.

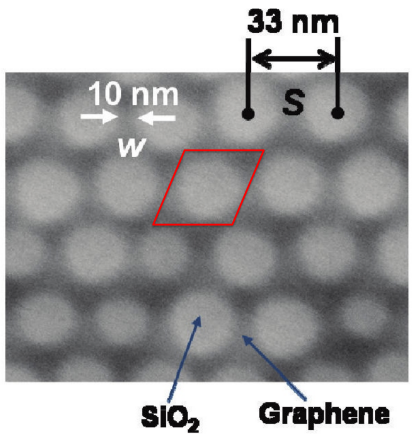

Fig. 2.11. SEM image of a graphene nanomesh with neckwidth of 10.0 nm (periodicity of 33 nm) ref. [19] (Red box shows roughly a unitcell)

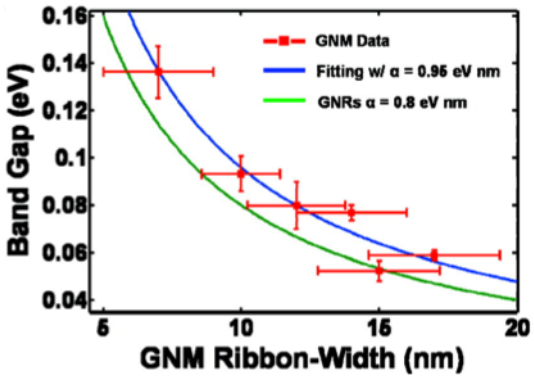

Fig. 2.12. The energy bandgap Eg versus the average GNM ribbon-width w (square). Taken from ref. [19]

In order to reveal the essential relation between the bandgap and neckwidth, a good starting point is to model a small GNM structure with controlled number of atoms removed. Afterwards, we will attempt to model the experimental structure described in Fig. 2.11 and compare with their results shown in Fig. 2.12.

The first structure to be studied is shown in Fig. 2.13 (a). Neckwidth, marked as 'W' in the figure, is the shortest distance between neighbor holes. The supercell structure contains 12 x 12 graphene primitive unitcells, as shown in Fig. 2.13 (b), the hole size is varied in order to investigate its effects on bandstructure. The edges on the hole are passivated with hydrogen atoms.

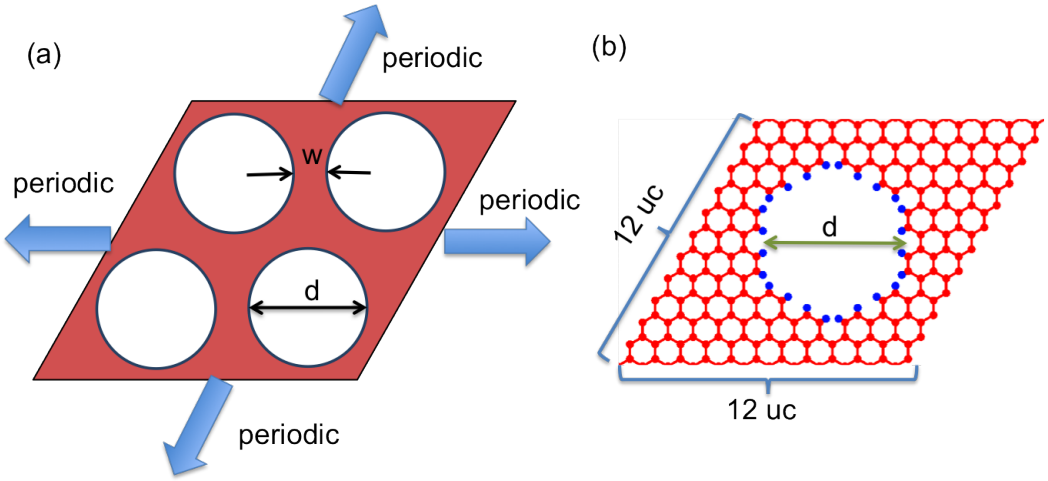

Fig. 2.13. (a) The periodic structure of GNM. 'd' is the hole diameter and 'W' is the neckwidth. (b) A supercell containing 12 x 12 graphene (red) primitive unitcells. Hole diameter 'd' is varied. Edges are passivated by hydrogen atoms (blue).

The bandstructure calculated for Fig. 2.13 structure with different hole sizes (in terms of uc, number of primitive unitcells) are compared in Fig. 2.14. As shown in the figure, the bandstructure for a GNM with circular hole indeed possesses a bandgap. The size of the bandgap increases with the hole size, as shown, from 0.29 eV at d = 3 uc to 0.75 eV at d = 7 uc. This trend of bandgap is expected, since a larger hole narrows the path that electrons can travel through, effectively increases the spacial confinement, and as a result, the bandgap increases. However, as the hole size becomes large, as shown in the d = 7 uc case, some dispersionless bands appears in the middle of the bandgap (marked by red circles). The next step is to take a close look at those dispersionless bands in order to understand their nature.

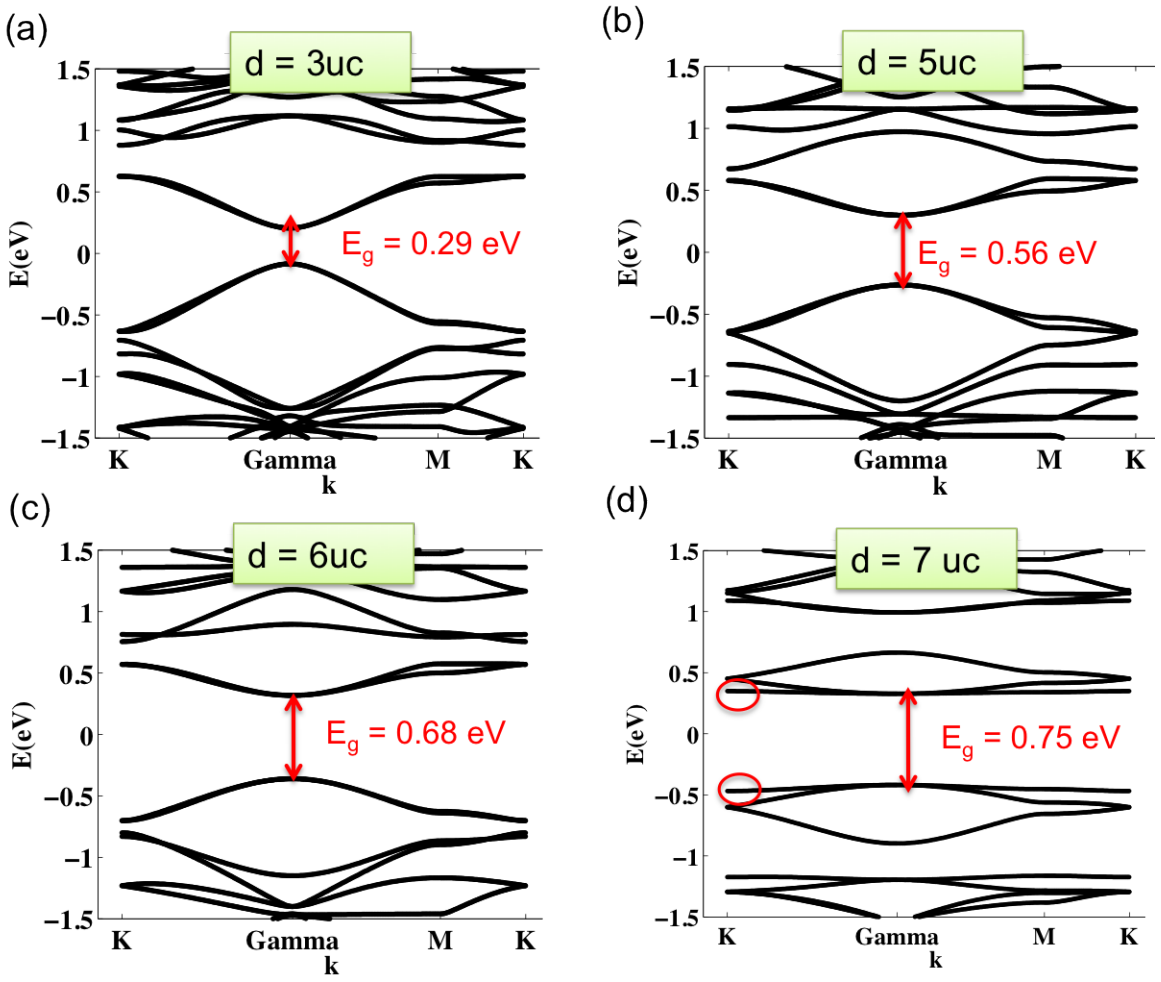

Fig. 2.14. Bandstructure calculation for Fig. 2.13 structure with different hole diameters (a) 3; (b) 5; (c) 6; (d) 7 (number of primitive unitcells in graphene)

The electron wavefunction magnitude $|\psi^2|$ at the Γ point of a dispersionless band is plotted in Fig. 2.15 (c). The plot clearly shows that the flat band is an edge state, whose electron wavefunction is localized on the hole edges. For comparison, Fig. 2.15 (b) plots wavefunction magnitude at the Γ point of a dispersion band, which is spread out in the entire structure. Upon a closer look, it is found out that the wavefunction of the edge state shown in (c) is only localized at the certain portions of the edges which have zigzag shape. One thing to emphasize is that the edges are already passivated

by hydrogen atoms explicitly in the p/d model. Therefore, these edge states are not because of dangling bonds on the edges. It can therefore be deduced that the zigzag geometry of the edges contributes to the localized states in the bandstructure.

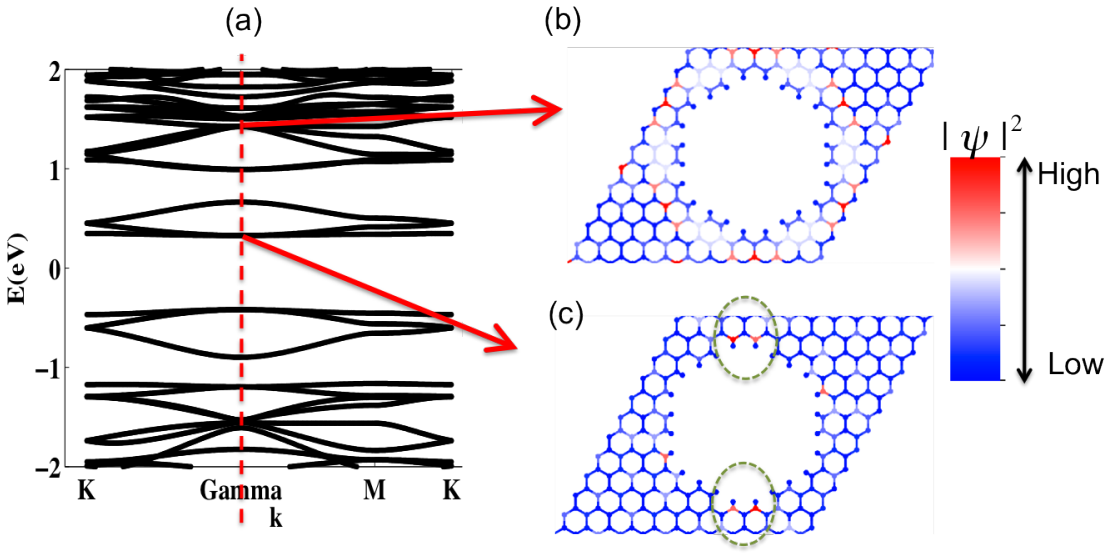

Fig. 2.15. (a) Bandstructure of GNM with d = 7uc (same as Fig. 2.14 (d)). Plot of electron wavefunction magnitude $|\psi^2|$ at Γ point of (b) a dispersion band and (c) a dispersionless band. Green circles in (c) marks the the zigzag edges on which the wavefunction is localized

Fig. 2.16 plots the bandgap versus neckwidth for GNM with various hole sizes. As shown by the red fitted line, when the neckwidth is large (small holes), the bandgap increases almost linearly with reducing neckwidth. However, the bandgap results at the small neckwidth range (large holes) deviates from the linear trend. This is because as the hole becomes larger, the edge effects (mostly due to the zigzag edges, see Fig. 2.15 above) becomes more dominant, and as a result, more flat bands are induced in the bandstructure. These flat bands must be excluded since they have little contribution to the electron conduction. However, the existence of flat bands due to the edge effects in big holes makes the bandgap calculation largely inaccurate.

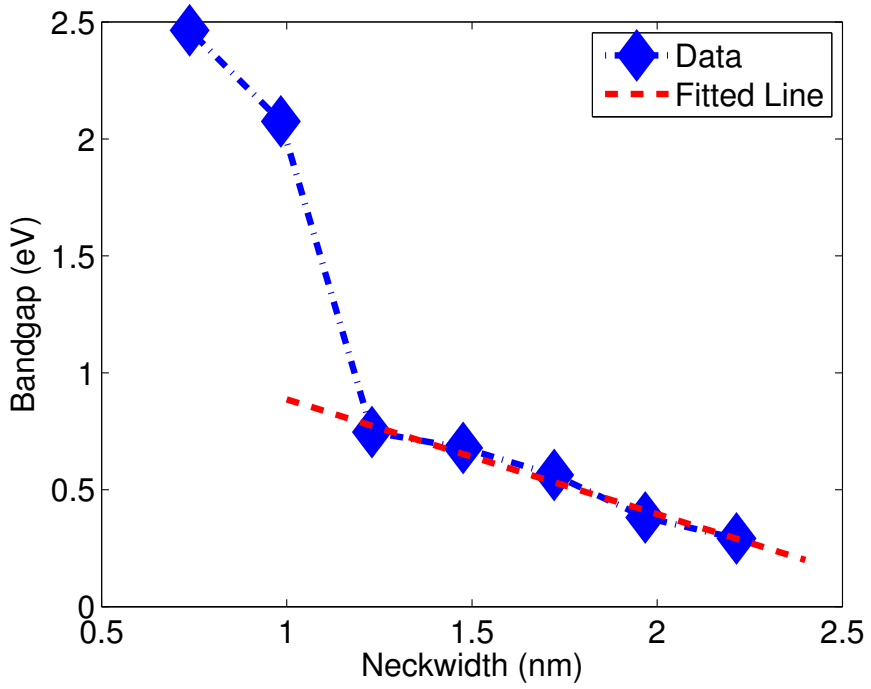

Fig. 2.16. Bandgap vs. neckwidth calculated for the structure in Fig. 2.13. Bandgap is almost linearly dependent on neckwidth at large neckwidth (small holes) range. Red dashed line is a linearly fitted curve. As neckwidth becomes small, the bandgap deviates significantly from the linear trend, this is because of the increased edge effects in large holes.

The next task is to model the experimental structure in Fig. 2.11, calculate the bandgaps at different neckwidths and compare them against the experimental results. Fig. 2.17 displays a supercell constructed in NEMO5 which resembles the experimental structure. It is is 33 nm long, which is about 138 graphene unitcells. Width of the circular hole at the center of the structure is varied.

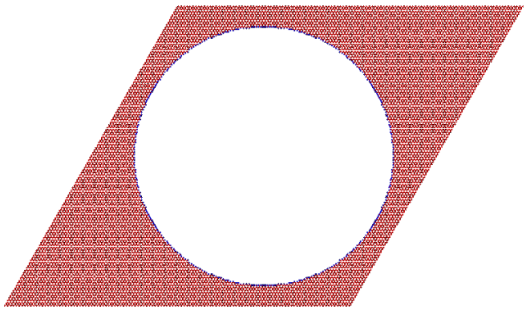

Fig. 2.17. Supercell of a circular-hole GNM example. The size of the supercell is 138×138 graphene unit cells, and it contains a circular hole at the center.

The bandgap vs. neckwidth for is calculated and plotted in Fig. 2.18, together with the experimental measurements from Fig. 2.12 for comparison. It can be seen that although our simulation results display similar trends as the experimental results, i.e. the bandgap increases as GNM neckwidth reduces, we cannot obtain a close quantitative fit. This is again due to the strong edge effects in this big structure, which induces bands with low dispersion, making it difficult to calculate the bandgap accurately. Despite such inaccuracies, both experimental measurements and simulation results suggest that GNM indeed has a bandgap that can be tuned by the neckwidth.

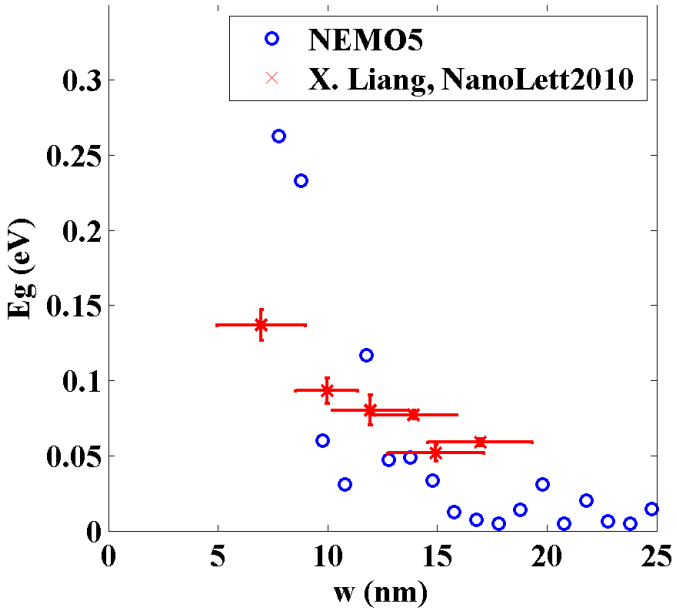

Fig. 2.18. Plot of bandgap in circular-hole GNM as a function of neck-width. Blue circles are NEMO5 calculation, in comparison with experimental result (red cross) from Liang et al. paper [19]

To illustrate the edge effect, we pick out a GNM sample with 9.7 nm neckwidth (d = 24 nm), and plot its bandstructure in Fig. 2.19 (a). A bandgap is observed with two flat bands in the middle. The electron wavefunction magnitude $|\psi^2|$ at the Γ point on one of the flat bands is shown in Fig. 2.19 (b), which indicates that electron wavefunction is localized on several 'puddles' at the edge. A zoomed-in plot on one of the puddles, shown in Fig 2.19 (c), reveals that it is localized on the zigzag edge, consistent with previous observations (Fig. 2.15).

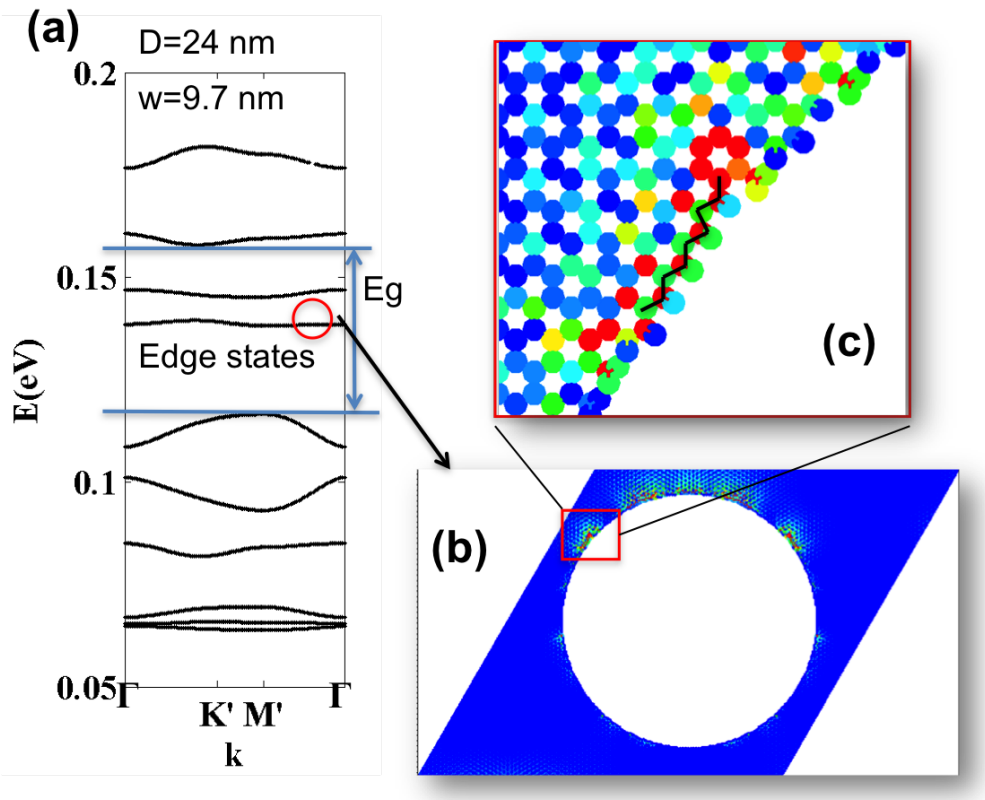

Fig. 2.19. An example showing the localized edge state. (a) Bandstructure of GNM, hole diameter d=24 nm. The bandgap is marked as E_g, which does not count the two edge states. The red circle indicates an edge state, of which the electron wavefunction is plotted in (b). The wavefunction shows that the electron at such an edge state is localized on the edge of the structure as 'puddles'. (c) Zoom in on one electron 'puddle', which shows that electron is localized on the zigzag edges.

From the study of GNM with circular shaped holes, it is learned that periodic perforation in graphene can open up a sizeable bandgap, which makes GNM a suitable candidate for transistor applications. Furthermore, the magnitude of bandgap can be tuned with different hole sizes, which makes it even more attractive for engineering of novel devices. However, it is also found out that the bandstructure is sensitive to the exact edge geometry of the hole. In the next section, the effect of hole shape on

the electronic properties of GNM will be investigated and the edge effects will also be studied in greater details.

2.3.2 Rectangular Hole Structures: Bandstructure vs. Edge Geometry

One of the key information obtained from the circular hole GNM study was that electrons tend to localize on the edge of GNM and that edge structures play a key role in the properties of GNM. In order to further understand the influence of edge geometry, or even make use of such electron preference for certain edge geometries, further study on different hole structures is necessary. To study the edge effects, two different types of edge structure, zigzag and armchair, must be separated and controlled. The circular hole GNM is no longer suitable for such a study because the edges on a circular hole are a mixture of zigzag and armchair structures.

A GNM with a rectangular hole, see Fig 2.20, is a natural choice for the next study, since the two pairs of sides always have different edge orientations. As for this study, the structure is oriented such that the zigzag edges always lie along the [100] direction, and armchair edges along the [010] direction. The degree of edge influence can be tuned easily by changing the dimension of the rectangular hole. The two particular structures for this study are shown in Fig 2.20(a) and (c). Both have 8×8 nm^2 supercells with a 1×7 nm^2 hole. For one structure as shown in (a), the long edge lies along [010], which has armchair shape, while the other structure in (c) has a zigzag edge as the long edge. For convenience, we call the structure in (a) armchair graphene nanomesh (AGNM), and the structure of (c) zigzag graphene nanomesh (ZGNM). The two structures are set up such that the only major difference is the dominant edge geometry. For AGNM, the edges are dominated by armchair edges and for ZGNM, the edges are mostly ZGNM. With this approach, the role of edge geometry can be clearly observed through bandstructure comparisons. The bandstructures for both structures along directions [100] and [010] and their respective structures are shown in Fig 2.20.

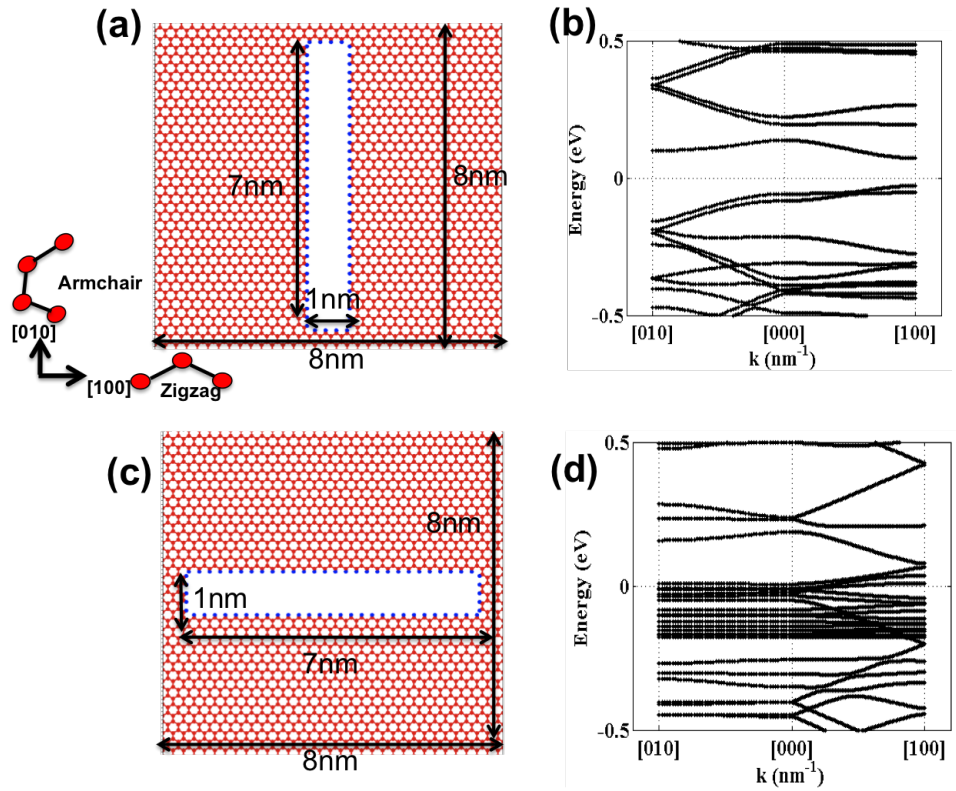

Fig. 2.20. (a), (c) structure of 8×8 nm^2 GNM with two different rectangular holes. Hole dimension: (a) 1×7 nm^2 (b) 7×1 nm^2. Edges are zigzag along [100] and armchair along [010]. (b), (d) Comparison of bandstructure for these two structures. Bandstructures in both cases show anisotropic dispersion along [100] and [010]. The dispersion difference is larger for structures with zigzag dominated edges, which is the case in the 7×1 nm^2 hole structure. The effects of such anisotropic dispersions on electron transport will be shown next.

Three main observations can be made from the bandstructure plots. First of all, the bands along two directions have very different dispersion, and along the long edge direction([100] for (b), [010] for (d)) dispersion is always much higher compared to the short edge direction. A high E-k dispersion means high electron velocity, which is a strong indication of good transport properties. Such anisotropic dispersions indicates that edge orientation does not only play a strong role in electronic structure, but may also effect the transport properties of GNM. The transport properties will be

discussed in the next section. Secondly, the ZGNM bandstructure exhibits a lot more flat bands than the AGNM bandstructure. These flat bands are localized edge states which have been discussed in the previous section. Thirdly, for the ZGNM case, the difference in dispersions along the two directions is much more pronounced. As can be seen in (d), the bands along [010] are mostly flat while the bands along [100] have large dispersion. In comparison, bands in AGNM (b), have reasonable dispersion along both directions. Origins of these observations will be further investigated later.

2.3.3 Rectangular Hole Structures: Edge Localization

From the bandstructure calculation for rectangular hole GNM, it is shown that GNM with different edge orientation, i.e, AGNM versus ZGNM, have very different electronic properties. In order to find out the origin of such edge dependent properties, the next logical step is to study the electron wavefunctions to see how the edge influence electron localization.

The two previous examples, AGNM and ZGNM, are studied individually. First we will study the ZGNM. Fig. 2.21 (c) shows the bandstructure of a ZGNM in Fig 2.20(c), and zoom in on a portion of the bands marked in the red box and displays it in Fig 2.21(a). As can be seen from the zoom in plot that most of these bands are flat. We pick two of these flat bands and plot the electron wavefunction at Γ point and display them in (b) and (d). The wavefunction plot shows that the electron at these flat bands is strongly localized on the zigzag edges, which again confirms that these flat bands are localized edge states.

Next we turn our focus to AGNM(shown in fig 2.20(a)). Fig. 2.22 plots its bandstructure and a zoomed-in portion. The electron wavefunction at the Γ point of two bands is plotted and shown in (b), (d). In this case, the bands are not as flat, which means that the electrons are no longer strongly localized. The electron wavefunction plot confirms this argument by showing a more spreadout wavefunction. However, although the zigzag edges along [100] direction are just a small portion of

the entire edge structure, there is still localization (but not as strong) present along the zigzag edges. The fact that the electron wavefunction localizes on the zigzag edge in such an armchair dominant structure is a strong supporting fact for the argument that zigzag edge is more preferred by electrons.

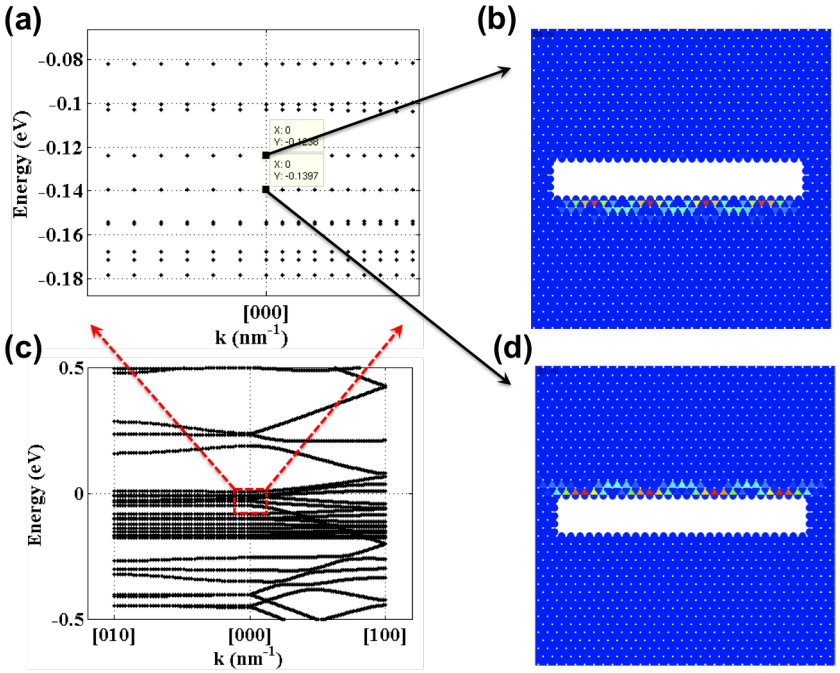

Fig. 2.21. (a), (c)Bandstructure plot of 8×8 nm^2 GNM with 7×1 nm^2 hole (Fig. 2.20(c)) (a) is zoomed in plot for bands marked by red box in (c), most of these bands are flat, which means they are edges states. (b), (d) electron wavefunction plot at Γ([000]) points of two flat bands. It can be seen that the flat bands are indeed localized edge states, as wavefunction is concentrated on the zigzag edge.

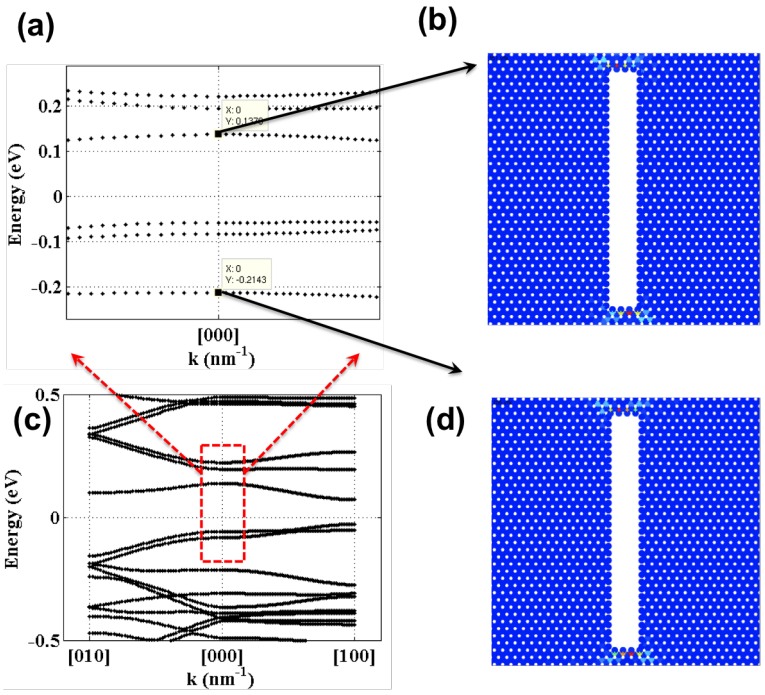

Fig. 2.22. (a), (c)Bandstructure plot of $8\times8nm^2$ GNM with $1\times7nm^2$ hole (Fig. 2.20(a)) (a) is zoomed in plot for bands marked by red box in (c). (b), (d) electron wavefunction plot at Γ points of two bands. Even if these two bands are not localized, the electron wavefunction is still denser at the short zigzag edges. From this it can be concluded that electron prefers to localize at the zigzag edge.

2.3.4 Rectangular Hole Structures: Anisotropic Conductance

In order to see the edge effect on electron conduction, transport calculation must be performed for GNM with rectangular holes. Fig 2.23 shows the setup for the transport calculation of a ZGNM along the [100] direction. Source and drain are exact same structure as the device. Electrons enter through the source-device contact into the device and leave the device via the device-drain contact. The electron transmission function $\bar{T}(E)$ is then calculated using the non-equilibrium Green's function(NEGF) method, which is described as:

$$\bar{T}(E) = Trace[\Gamma_1 G \Gamma_2 G^{\dagger}] \tag{2.15}$$

where G is the Green's function that has expression:

$$G(E) = [EI - H - \Sigma]^{-1} \tag{2.16}$$

where E is energy, I is the identity matrix, H is the device Hamiltonian, and Σ is the contact self-energy. Γ can be obtained from Σ using the identity:

$$\Gamma = i[\Sigma - \Sigma^{\dagger}] \tag{2.17}$$

Details of NEGF formalism can be found in professor Datta's book [21].

Transmission function has fundamental connection to the electrical conductance, which can be seen shown in the following relation:

$$G = \frac{q^2}{h} \int_{-\infty}^{\infty} \bar{T}(E)(-\frac{\partial f_0}{\partial E}) dE \tag{2.18}$$

where G is the conductance, $\bar{T}(E)$ is the transmission function and f_0 is the Fermi function which has the form:

$$f_0 = \frac{1}{1 + e^{(E-E_f)/k_B T_L}} \tag{2.19}$$

Therefore, by calculating and analyzing the transmission functions $\bar{T}(E)$ in various GNM structures, it can be deduced whether or not a certain type of structure has good electron conductance along a certain direction.

Fig. 2.24 plots the electron transmission for the ZGNM structure shown in Fig. 2.20(c) at zero bias along both [100] and [010] directions. For comparison, the band-structure is also plotted. The results show a much larger transmission along the [100] direction than [010] direction, which coincide with the fact that the band dispersion along the [100] direction is much larger. Such a match between band dispersion and electron transmission is expected, because the transmission function $\bar{T}(E)$ could also

be written as multiplication of $T(E)$ and number of modes $M(E)$. $T(E)$ is the probability that an electron at energy, E injected from source contact exits in drain contact (or vice versa) and is given as the following relation:

$$T(E) = \frac{\lambda(E)}{\lambda(E) + L} \tag{2.20}$$

where λ is the mean free path of electron and L is the device length. $M(E)$ is given as:

$$M(E) = W \cdot M_{2D}(E) = W \cdot \frac{h}{4} < V_x^+(E) > H(E - E_c) \tag{2.21}$$

From the above equations, it can be seen that the transmission function $\bar{T}(E)$ is directly related to the average electron velocity in the transport direction $< V_x^+(E) >$, which is also related in the band dispersion since $v_x = \partial E / \partial k_x$. Therefore, large band dispersion results in large electron velocity, which in turn leads to a large electron transmission and conductance.

Same calculation on the AGNM structure (Fig. 2.20(a)) also reveals similar features, as shown in Fig. 2.25 that transmission along the [010] direction is much larger.

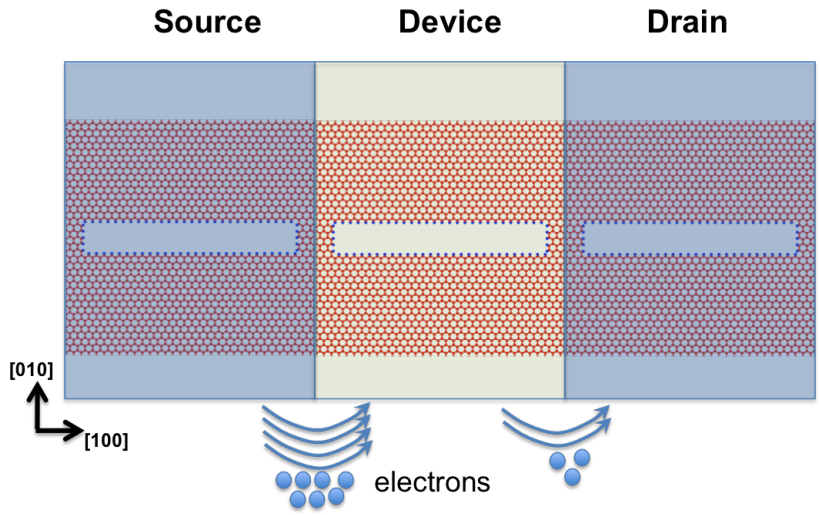

Fig. 2.23. Diagram for tranport calculation setup along [100] direction for rectangular hole GNM. Source, drain are made of the exact same structure as the device

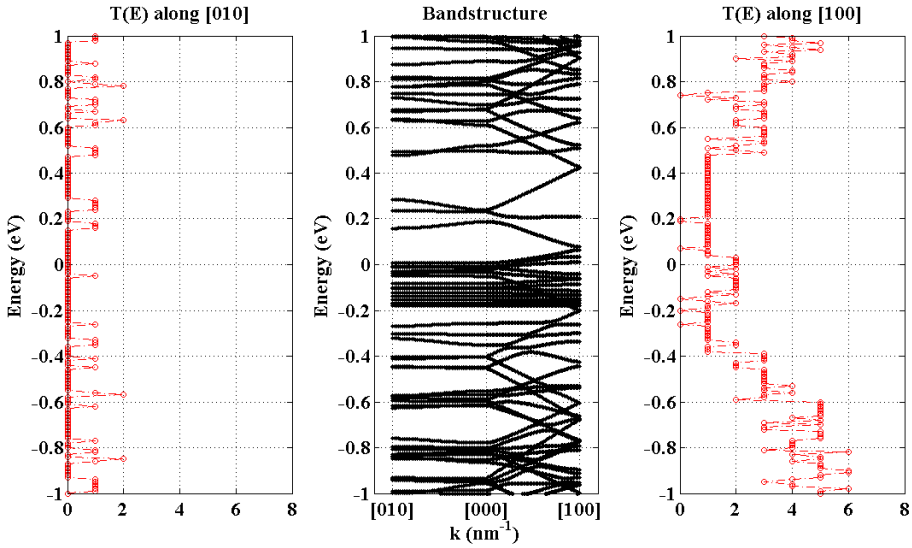

Fig. 2.24. (Middle) Bandstructure for 8×8 nm^2 GNM with 7×1 nm^2 hole (Fig 2.20(c)) (Left) Electron transmission along [010] direction (Right) Electron transmission along [100] direction. Transmission along the long edge direction, which in this case is [100], is much larger than the other direction.

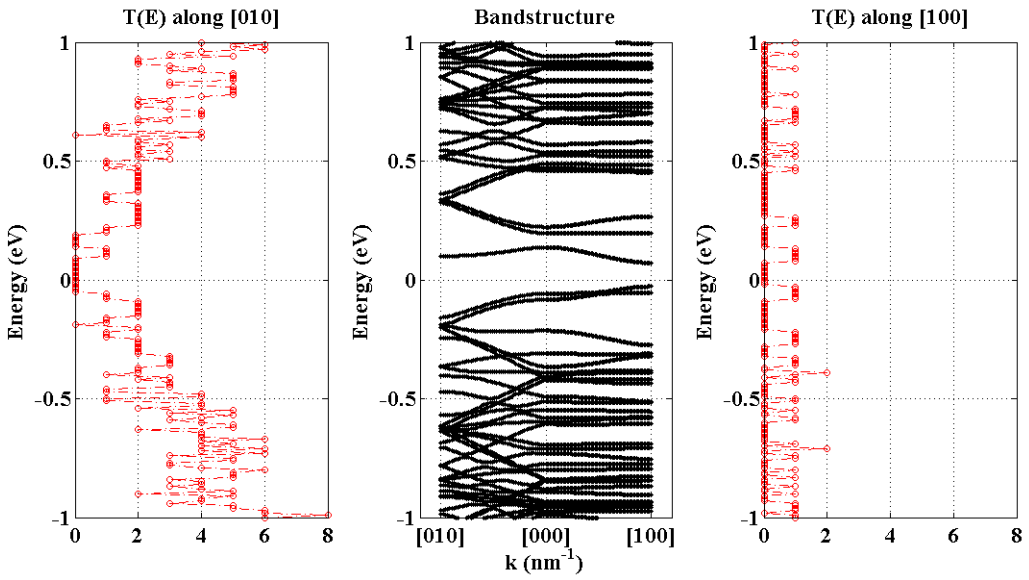

Fig. 2.25. (Middle) Bandstructure for 8×8 nm^2 GNM with 1×7 nm^2 hole (Fig 2.20(a)) (Left) Electron transmission along [010] direction (Right) Electron transmission along [100] direction. Transmission along the long edge direction, which in this case is [010], is much larger than the other direction.

2.3.5 Rectangular Hole Structures: The Edge Effect on Conductance

At this point, we can conclude that the edge structure in GNM plays an important role in electron conductance and that electrons prefer to localize on the zigzag edge. However, one important question remains: how does the electron preference on the zigzag edge affect electron transport? In order to answer this question, a third structure has been studied. This structure, as shown in Fig. 2.26 has the same supercell size of 8×8 nm^2, but the hole size has been changed to 4×4 nm^2. In this case, it is a symmetric structure, with same lengths of armchair and zigzag edges. Therefore, any difference in electronic structure and transmission along two directions can be accredited to the edge structure. The same calculations are performed on this structure as for the previous examples. Fig. 2.27 plots the bandstructure as well as the electron wavefunction on two bands. In this case, the electrons again are strongly

localized on the zigzag edges. From the bandstructure, it can be observed that the dispersion along [100] is higher. Transmission along [100] and [010] is calculated and plotted in Fig 2.28. [100] and [010] transmissions are plotted on top of each other for comparison. It can be clearly seen that the [100] direction has a higher transmission than [010]. Such difference can be explained by the electron preference on the zigzag edges, which is illustrated in Fig. 2.29. Electrons tend to localize on the zigzag edges, forming puddles, which is marked as yellow color on the figure. Such localization along [100] edges makes it easy for electrons from one cell to travel along [100] directions to the next cell. In comparison, traveling along the [010] requires electron to tunnel through the hole, which is a more difficult process. As a result, transmission along [100] is stronger than [010].

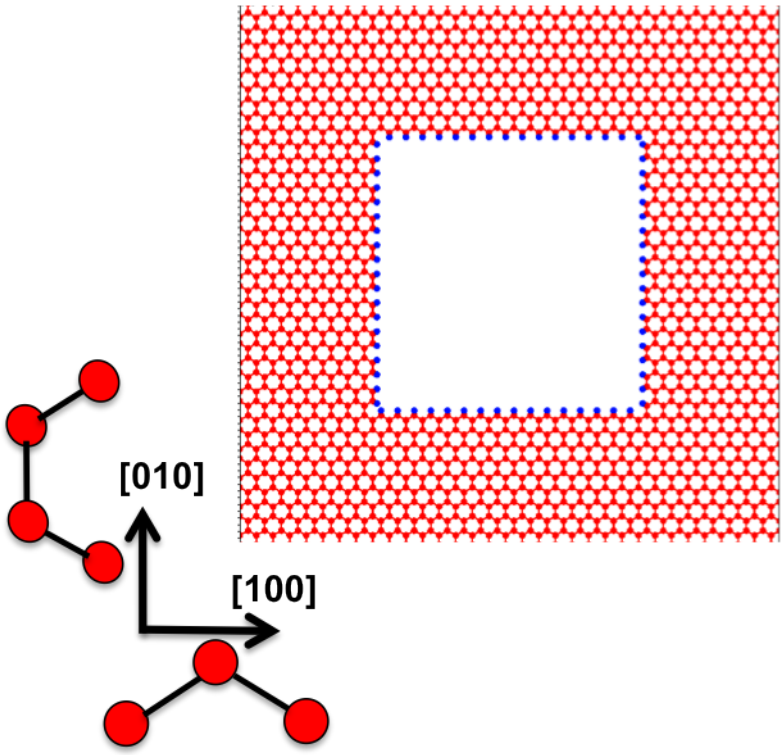

Fig. 2.26. Structure of 8×8 nm^2 GNM with 4×4 nm^2 rectangular hole. Edges are zigzag along [100] and armchair along [010]

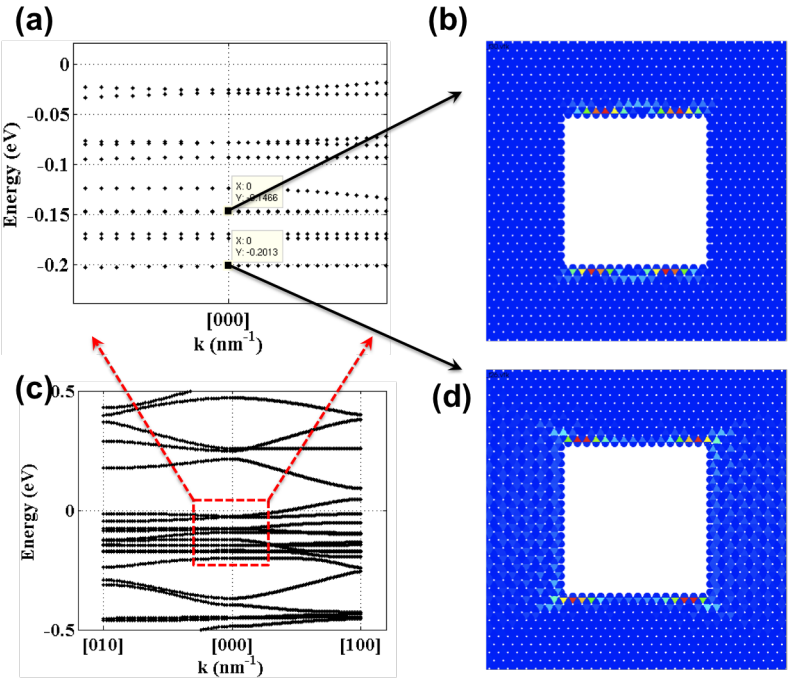

Fig. 2.27. (a), (c)Bandstructure plot of 8×8 nm^2 GNM with 4×4 nm^2 hole (a) is zoomed in plot for bands marked by red box in (c). (b), (d) electron wavefunction plot at Γ points of two bands. In this case, this structure has symmetric geometry, yet the wavefunction still concentrates on the two zigzag edges. This is another prove that electron prefers to localize at the zigzag edge.

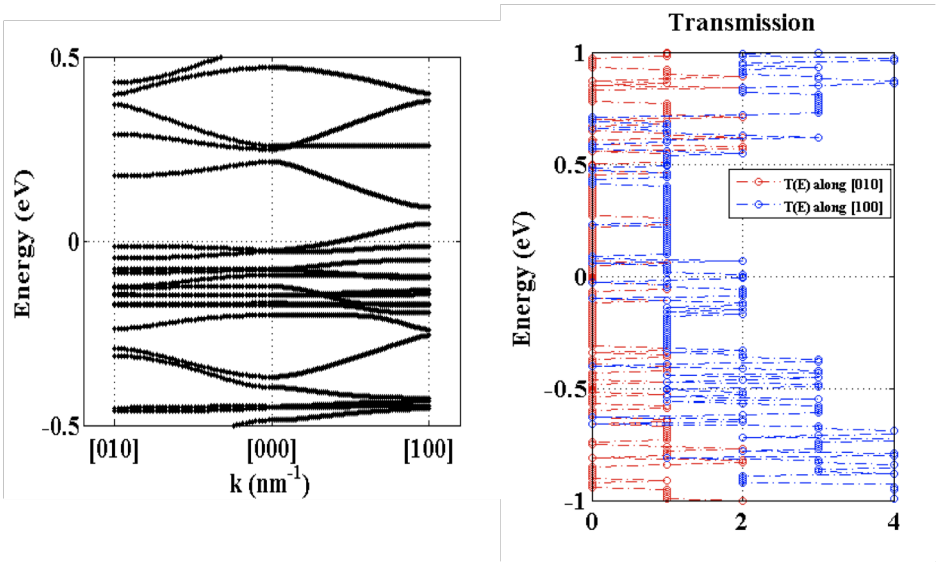

Fig. 2.28. (Left) Bandstructure for 8×8 nm^2 GNM with 4×4 nm^2 hole. (Right) Comparison of transmission along [100](blue) and [010](red) directions. In this case, this structure has symmetric geometry. The transmission along [100] is higher than [010] direction. Such difference is due to electron preference of zigzag edges ([100]) ever armchair edges ([010]).

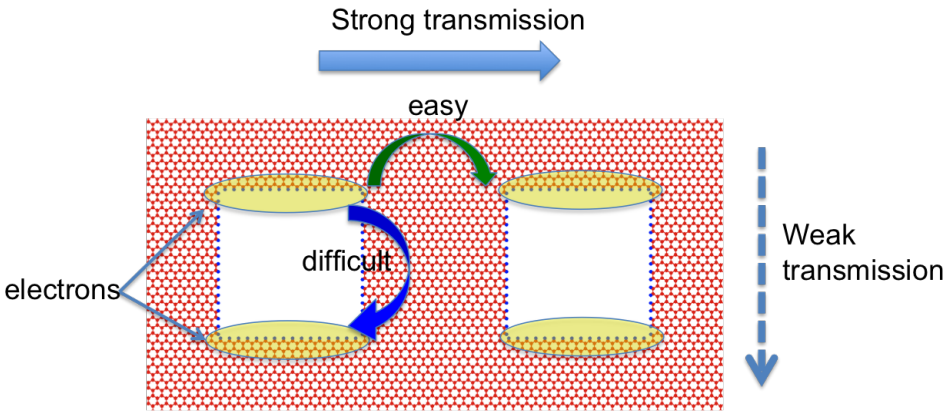

Fig. 2.29. Illustration of electron localization effect on conductance. Electrons tend to localize on the zigzag edges, forming puddles, which is marked as yellow color on the figure. Such localization along [100] edges makes it easy for electrons from one cell to travel along [100] directions to the next cell. In comparison, traveling along the [010] requires electron to tunnel through the hole, which is a more difficult process. As a result, transmission along [100] is stronger than [010].

2.3.6 Rectangular Hole Structures: Proposal of Novel Devices

Through the simulation study presented in this work, some interesting and special properties have been found on rectangular graphene nanomeshes. One such properties is the anisotropic electronic conductance along different directions. What makes these structures even more intriguing is the strong dependence of their electronic properties on geometries, including hole size, shape, orientation, as well as edge geometries. These properties open up enormous opportunities and freedom for bandstructure engineering in graphene, which greatly expand the already tremendous potential of graphene based applications. Below are some application ideas based on the study of GNM, which the authors deem worthy of further investigation.

- Band-to-band tunneling transistors: GNM can potentially find ways into novel transistors applications due to their strong bandstructure engineering capabilities. Through bandstructure engineering, GNMs can be designed to be the

channel materials for different types of devices, such as GNM based field-effect-transistors (GNMFET) or band-to-band-tunneling transistors (BTBT).

- Quantum computing: There has been theoretical work on quantum wire-based qubits [25] by Zibold and Vogl. In that work, they have proposed the use of quantum wires with coupling windows to form a qubit, and they also demonstrated that the entanglement can be controlled externally by tuning the tunneling coupling between wires. However, due to the complexity of the system, it was never put into real experimental tests. The rectangular hole GNM structures presented in this work, on the other hand, can be treated as arrays of nanowires, with strong conduction along the hole direction(see fig. 2.29). The weak conduction along the other direction, on the other hand, can be thought of as coupling between the wires. If such coupling can be tuned through external methods such as electrical field, then GNM conceptually can work as a platform for quantum-wire based spin qubits.

2.3.7 Conclusion

The electronic structure simulation on circular hole GNM shows that a tunable bandgap can indeed be obtained by varying the GNM ribbon neckwidth. This conclusion is in agreement with experimental studies suggesting GNM's potential for being used in digital logic devices. Further study on the rectangular hole GNM with two different edge structures, AGNM and ZGNM, shows that the edges plays a role as electron 'guide', which allows electrons to travel much easier along the dominant edge direction. Electron preference for zigzag edges suggests that the ZGNM is a better electron conductor than AGNM. Further transport calculations with biased potential are necessary to demonstrate the potential of GNM devices for real applications.

3. ATOMISTIC MODELING OF A TUNABLE SINGLE-ELECTRON QUANTUM DOT IN SILICON

3.1 Introduction

3.1.1 What is Quantum dot

Quantum dots (QDs), also known as artificial atoms, have drawn enormous interest recently due to their potential application in solid-state quantum computing. A quantum dot can be described as a confined semiconductor structure in all three spatial dimensions. Quantum dots allow confinement of countable number of electrons, while preserving their spin information. The capability of storing and manipulating electron spin information makes quantum dots a promising candidate for spin qubits in quantum computing. Depending on how the confined space is created, there are several types of quantum dots. One type of quantum dot is a single donor quantum dot, such as a Si:P quantum dot [49]. In the Si:P quantum dot, the spatial confinement is created by the donor potential of a single phosphorous atom. Another type of quantum dot is the electrostatically defined quantum dot, where the confinement is created by electric fields controlled by gate biases. Both types of quantum dots have been studied experimentally and proposed as the platform for spin qubits in a future quantum computer [49] [40].

3.1.2 Advantages of Si MOS Quantum Dot

Among all the semiconductor materials, Si in particular is a favorite candidate for fabricating QDs for quantum computing devices. The main reason is the fact that Si has a long spin coherence time [26] [28] [29], which is the direct measure of how long a spin qubit is able to preserve its quantum information. A long spin-coherence time

means that electrons Si quantum dots are less likely to lose their spin information due to interaction with the external world, which also means that a Si based qubit is capable of performing more operations per second before losing its spin information. Another significant advantage of silicon is that over 90% of the isotopes in nature have zero net spin ($^{28}Si, I = 0$), and with additional purification processes, the composition of ^{28}Si can be upgraded to up to 99.9% [27]. Having an environment with zero net spin significantly reduces decoherence for spin based qubits. Moreover, silicon metal-oxide-semiconductor (MOS) structures have been the dominant transistor design in the semiconductor industry over the last several decades. Using existing state-of-the-art Si MOS technology for quantum computer designs will definitely make it easier for future circuit integration.

3.1.3 What Is Valley Splitting and Why Is It Important

Despite the many advantages of Si, there are some disadvantages when it comes to qubit design. One of the major hurdles for Si based qubit designs is the six-fold valley degeneracy in Si. As mentioned before, one of the most important issues in spin qubit design is controlling spin-decoherence. Decoherence is an irreversible process that happens when the qubit interacts with the external environment, causing the electrons in the qubit to lose their spin information. For a quantum dot qubit, it is required that the lowest two spin states are well-separated from other states to avoid quantum decoherence [30] [31]. For silicon, the six-fold valley degeneracy poses a great challenge to provide such two-spin states that have large energy separation from other states, as is illustrated in Fig. 3.1. Fig. 3.1 shows the conduction band minima of Si. Because Si has six-fold degeneracy, the conduction band minima has six portions, each represented by a lobe located in [100] [010] or [001] directions. For bulk Si, all these six states are at exactly the same energy value. When an external bias is provided along [001] direction, the asymmetry in external potential will cause the six-fold degeneracy to split. The energy position of a certain state is determined

by the confinement strength in that direction. Similar to the quantization states in a quantum well, the energy of a state is inversely proportional to the effective mass along the confinement direction. The two states along [001] direction have a larger effective mass than the four states in the direction transverse to the bias. Therefore, the two [001] states will have lower energies than the other states(along [010], [001]). Additional asymmetry effects in the quantum dot will further split the states by a few hundred meV. Due to spin degeneracy, each valley contains a spin-up and a spin-down state, forming a two-spin system. The energy difference between the lowest two valleys, also known as valley-splitting(VS), is a critical quantity to determine whether the QD is suitable for safely storing electron spin information.

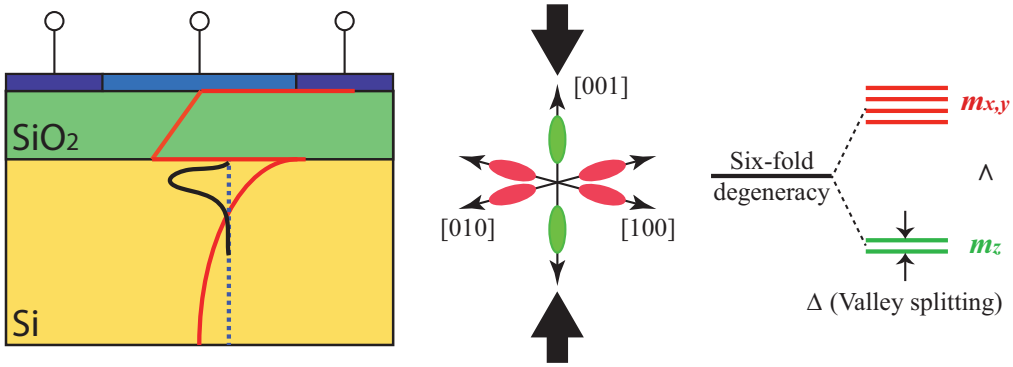

Fig. 3.1. (Left) Physical structure of a Si MOS QD. Red curve is the confinement potential along [001] direction. (Middle) Six-valley degeneracy diagram of Si, where each of the six lobes is a conduction band minimum of the Si bulk bandstructure. Two black arrows along [001] direction represent the confinement potential. (Right) Energy splitting diagram due to [001] confinement potential. Two green lines correspond to [001] direction states. Four red lines are the other four states along [010] and [001] directions.

Because of the significance of VS in quantum computing applications, it has been widely studied theoretically [32] [33] [34] [35]. Boykin et al. calculated VS in a silicon quantum well as a function of barrier height using a $sp^3d^5s^*$ tight-binding model [32] [33]. Boykin et al. concluded that VS is an oscillation function with QW width and

overall, decreases as with increasing QW width. Despite extensive theoretical work on VS, the actual VS values measured experimentally vary from micro-electron-volts to milli-electron-votes and differ from device to device [36] [37] [38] [39]. The reason for such differences is because VS has critical dependence on factors, such as electrical field, confinement strength, lattice miscuts, oxide interfaces and so on. Therefore when it comes to theoretical guiding of experimental design of QDs for QC devices, it is necessary to provide a range of VS values with respect to bias voltage through simulation.

3.2 Objective of This Work

3.2.1 Experimental Device of Interest

A major hurdle for creating silicon quantum dots for electron-spin qubits has been the difficulty to reduce the Si/SiO_2 interface disorder, which makes it difficult to achieve single-electron occupancy [41] [39]. However, recently Lim et al. have been able to fabricate a Si MOS based QD structure which has low Si/SiO_2 disorder [40], and proved that the device indeed could operate down to the single-electron regime. The Si MOS QD of interest is shown in Fig 3.2, from (a) the top view and (b) a cross-section view. The device operation is controlled by five independent gates. L1 and L2 control source and drain, respectively, and inject or extract electrons in and out of the quantum dot. B1 and B2 gates create the depletion region in the channel, which serves as a barrier for tunneling electrons. The plunger gate P at the top controls electron filling in the middle dot region by raising or lowering the energy level in the dot. Fig 3.3 shows the "Coulomb diamond" charge stability diagram, which plots the differential conductance dI/dV_{SD} of the device versus the plunger gate V_P and source-drain voltage V_{SD}. The edges of each "diamond" in the diagram show the transition voltages for one additional electron to enter in or exit out of the QD. From the figure, it is seen that the first diamond has completely opened up, showing clear diamond edges, and thus indicates that the transition takes place only when the last

electron tunnels in and out of the QS. Therefore, it can be concluded that the Si MOS QD device indeed can operate down to the single-electron regime.

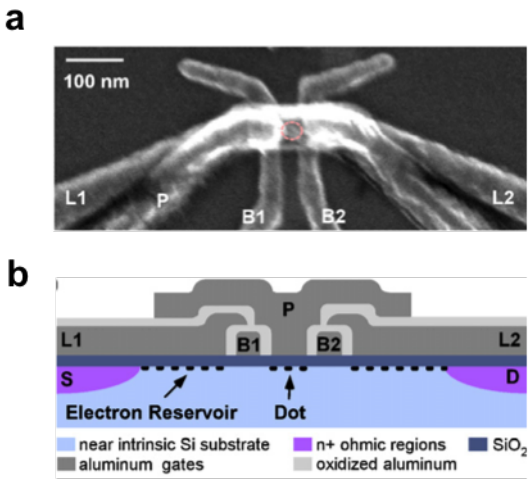

Fig. 3.2. (a), (b) Physical structure of Si MOS QD. Five top gates marked L1, L2, B1, B2, P are on top of the oxide interface to create electron reservoir (L1/L2), barrier between QD and the reservoir (B1/B2) and QD (P). Image taken from [40] with permission.

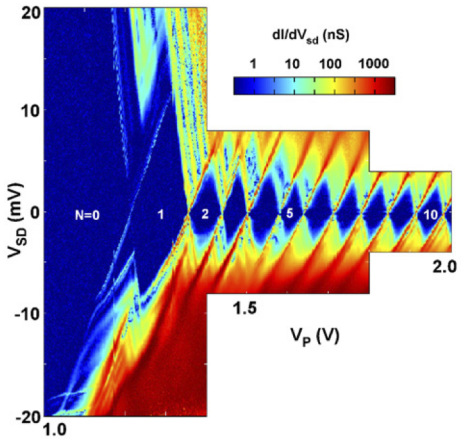

Fig. 3.3. Charge stability diagram of the Si MOS QD device in the few-electron regime. By decreasing the plunger gate voltage V_P, the electrons are depleted one-by-one from the dot through tunnelling. The first diamond opens up completely; indicating that the last and only electron has tunnelled out of the dot. [40]

3.2.2 What Needs To Be Studied

In order to decide whether or not this device is a suitable candidate for QC applications, knowledge of the valley splitting range inside this quantum dot under various gate biases is necessary. Below are several questions that experimentalists are particularly interested in:

- What are the combinations of gate bias voltages that result in a single electron in the quantum dot under equilibrium?
- What is the possible range of VS in the QD under proper biasing conditions?
- How does the VS depend on factors such as external field and barrier height?

The goal of this work is to seek answers to these questions and provide insight and guidance to experimental design of Si MOS QD devices, by using a modeling and simulation approach. This work was done in collaboration with an experimental

group, which also fabricated the device, at the Center for Quantum Computation and Communication Technology in Australia.

3.3 Methodology

3.3.1 Need for Atomistic Modeling and NEMO3D-peta

As was discussed above, the valley splitting is heavily dependent on various atomistic effects such as oxide interface roughness, lattice miscut, substrate orientation and so on. Therefore, in order to correctly model VS in the MOS QD, an atomistic approach is required to account for the various atomistic effects and quantum mechanical effects. Meanwhile, the QD device to be modeled contains at least several million atoms in Si bulk. Modeling such a large structure atomistically requires a massively parallelized simulator and abundant computing resources.

The Nanoelectronic Modeling Tool(NEMO 3-D) can simulate atomistic structures of realistic sizes and treats non-parabolicity of bulk materials using an empirical $sp^3d^5s^*$ tight-binding model [42] [43] [44]. NEMO3-D proved successful in several problems such as modeling of valley-splitting in miscut Si/SiGe quantum wells [45], InGaAs embedded InAs quantum dots and in the modeling of the spectrum of phosphorus impurities in silicon FinFETs [46].

NEMO3D-peta is a massively parallelized tool based on NEMO 3-D, and expanded the existing capabilities of NEMO 3-D with advanced parallelization schemes. NEMO3D-peta allows execution of self-consistent Schrodinger-Possion simulations on multi-million-atom structures within several hours using a couple of hundred cpu cores. Details of NEMO3D-peta's functional modules, parallelization scheme, benchmarking details and so on can be found in ref. [50]. NEMO3D-peta proved successful in modeling densely Phosphorous doped Silicon devices(Si:P), such as Si:P δ-layers [47], Si:P single atomic layer nanowires [48], and Si:P single atom transistors [49].

In this work, the Si MOS QD device will be studied using NEMO3D-peta and VS will be calculated under various bias combinations. The next section will explain in detail how the device is modeled and key results will be presented and discussed afterwards.

3.3.2 Simulation Domain

The physical structure of the Si MOS QD device is shown below in Fig. 3.4(a),(b) (same as figure 3.2). The device is controlled by five gates P, B1, B2, L1, L2 as explained before. The QD region, where electrons tunnel in and out of, is marked in the figure by the red box. The S and D regions are electron reservoirs, which provide electrons to the QD. The QD region is much smaller compared to the outside region. In this study, the objective is to calculate the VS when the device is in equilibrium and when there is only one electron in the quantum dot. Therefore, only the QD region needs to be included in the simulation domain while assuming that the source and drain set the Fermi level across the entire device. The QD region to be modeled by NEMO3D-peta is shown in Fig. 3.4(c) and (d). The domain is restricted to the central region of the device, which includes the dot and part of the left and right barrier regions. The SiO_2 thickness is roughly 10 nm. The oxidized aluminum surrounding each metal gate is ignored in the domain. The plunger gate region is roughly 30×60 nm^2. In order to investigate geometry effects on the VS, the width of the plunger gate is adjusted to four different values (Wc = 30, 40, 50 and 60 nm). The overall electronic domain is fixed to 60×90×40 nm^3 and contains roughly 8 million atoms.

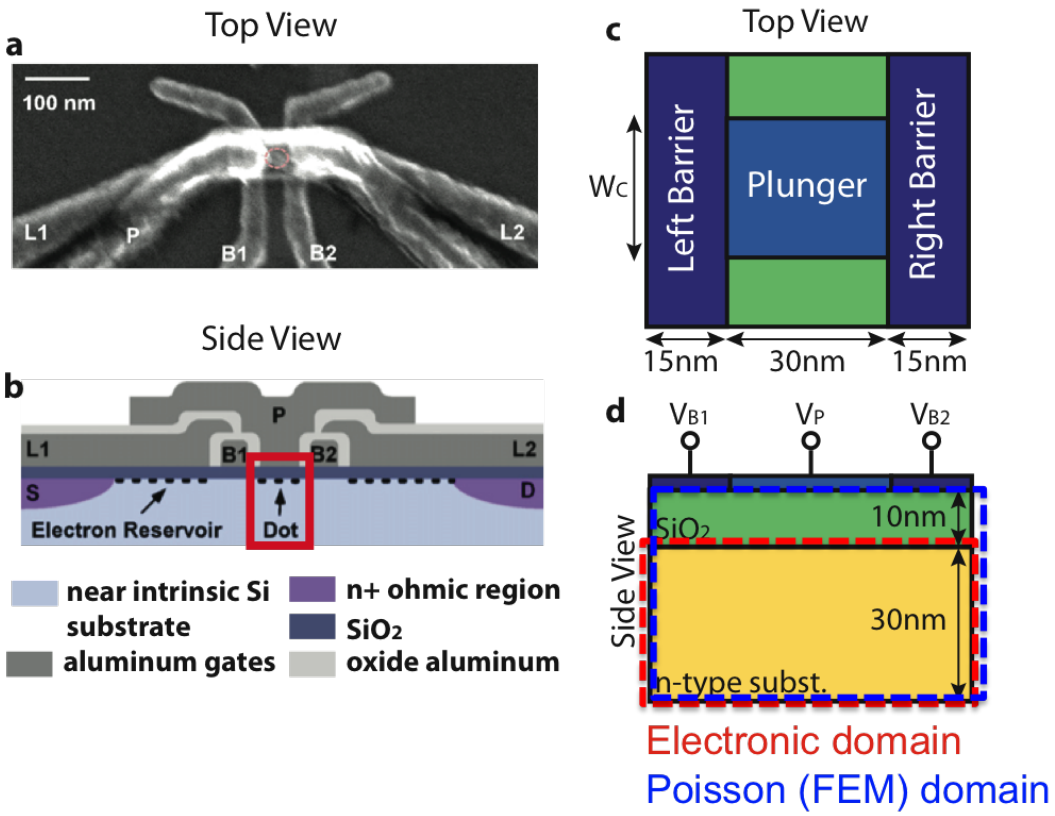

Fig. 3.4. Comparison of real device structure and NEMO3D-peta simulation structure. (a),(b) SEM images, same as in Fig. 3.2. (c) Top view of simulation structure, which shows only the dot region of the device. Left barrier, right barrier, plunger gates correspond to B1, B2 and P gates in (a) respectively. (d) Cross section view of simulation structure. The silicon substrate is 30 nm thick, which is included in the electronic domain of the Schrodinger solver. SiO_2 is 10 nm thick. The FEM domain for the Poisson solver includes the entire structure(Si plus oxide)

The entire device operates at extremely low temperatures of around 100 mK. At such low temperatures, the Fermi function, which determines which states are occupied by electrons, acts like a heaviside step function. States in the QD which are below the Fermi level will be occupied and states above Fermi level will be empty. Since each quantized state in the dot can occupy two electrons due to spin degeneracy, the Fermi level must cross exactly the ground energy state in order for the system to only contain one electron.

3.3.3 Simulation Scheme: Self-Consistent Loop

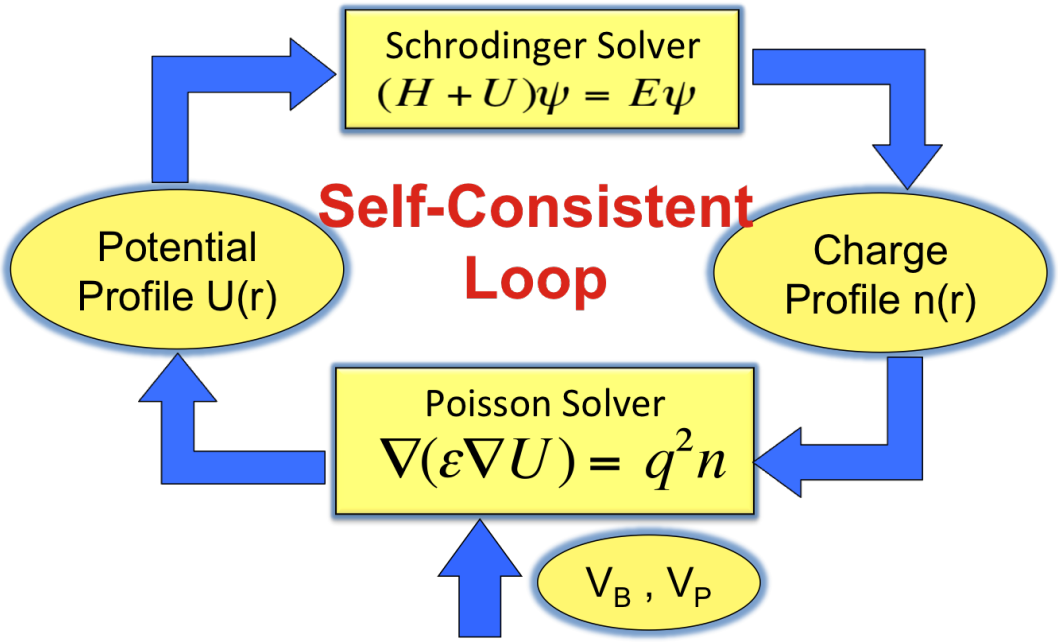

Fig. 3.5. Simulation scheme of NEMO3D-peta, which consists of a Schrodinger-Poisson self-consistent loop. The Schrodinger solver calculates eigenstates E and wavefunctions ψ by solving the $sp^3d^5s^*$ tight-binding Hamiltonian; the results E and ψ then go through charge integration process according to equation 3.1 to obtain the charge profile n(r); The Poisson solver takes the charge profile n(r), gate bias V_B and V_P as inputs and calculates the potential profile U(r) using Newton-Raphson method. The potential U(r) calculated from the Poisson solver then serves as the input to the Schrodinger Solver, and also marks the beginning of the next iteration cycle.

A Schrodinger-Poisson self-consistent simulation scheme shown in Fig. 3.5 is utilized to calculate the VS in the structure previously described. For a single iteration, the Schrodinger solver assembles the $sp^3d^5s^*$ tight-binding Hamiltonian of silicon substrate, then adds to it the potential profile of the device provided by the Poisson solver. After that it performs the eigenvalue calculation on the Hamiltonian matrix

to obtain the eigenstates (ϵ_i, ψ_i). The charge profile $n(r)$ is calculated by integrating the eigenstates with respect to the Fermi level of the device:

$$n(r) = 2\sum_i |\psi_i|^2 \frac{1}{1 + e^{\frac{\epsilon_i - E_F}{k_B T}}} \tag{3.1}$$

The Poisson solver takes the charge profile n(r) as its input and calculates the potential profile U(r) by solving the Poisson equation using Newton-Raphson's iterative method [51]. The boundary conditions on the top side of the substrate are determined by the gate bias voltages V_B and V_P, while all the other sides use Neumann boundary conditions, which specifies the electric field to be zero. The device Hamiltonian in the Schrodinger solver is then updated with the potential profile calculated from the Poisson solver, and again calculates the eigenstates for the next iteration.

In each iteration, convergence must be checked by comparing the updated potential profile with the old U(r) calculated from the previous iteration. If the difference is within the defined range of tolerance, then convergence is achieved and the final eigenstates are calculated using the Hamiltonian with the converged potential.

Since the entire simulation assumes low temperature (T $\approx$ 100 mK) to match experimental conditions, convergence is often difficult to achieve. The reason is that at very low temperatures, the Fermi function acts almost like a heaviside step function, and thus even small fluctuations in the potential profile may result in a huge differences in the convergence pattern. Fortunately, the VS values do not vary significantly when the simulation is close to convergence. Therefore, it is often necessary and practical to loosen the convergence criteria for a specific simulation in order to achieve convergence.

3.4 Results

3.4.1 NEMO3D-peta Scaling

Figure 3.6 shows the time it takes to perform the electronic structure calculation for a 60×90×40 nm^3 domain using different number of cpu cores. The domain size

is roughly 8 million atoms, which is a typical problem size in this work. The figure shows that NEMO3D-peta has exceptional scaling abilities, which is indicated by the almost ideal scaling curve. The efficient 3D spatial parallelization scheme has allowed the eigenstate calculation of 8-million atom structure to be performed in the range of hours.

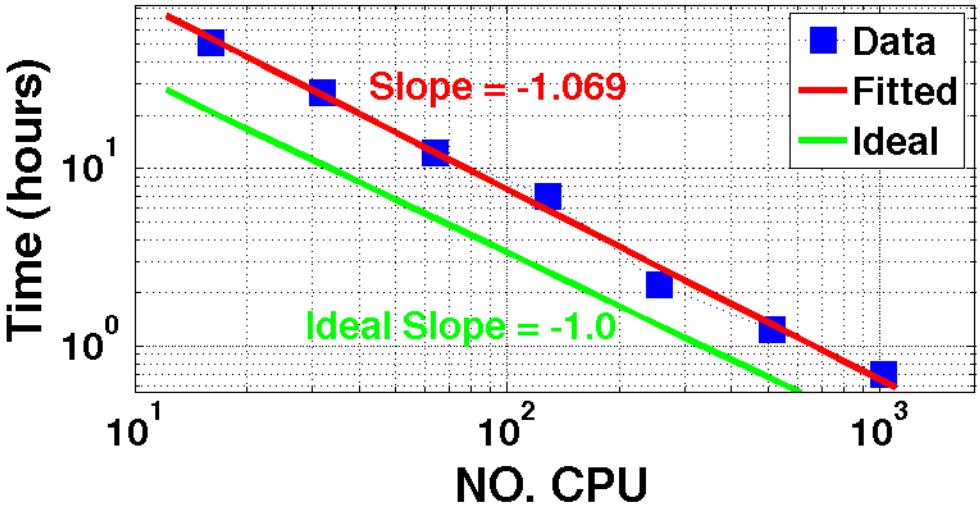

Fig. 3.6. Electronic structure calculation time as a function of the number of processors for a 60×90×40 nm^3 domain containing 8 million atoms.

3.4.2 Potential Landscape In the Single Electron Regime

As stated before, the objective of this work is to explore the VS behavior in MOS QD devices for various QD sizes and under various bias voltages, while maintaining a single electron in the QD. Therefore, the first main goal is to find out what the bias combinations are that lead to a single electron in the dot. Fig. 3.7 shows the relation of the plunger gate bias V_P and barrier bias V_B (in this case, two barrier gates have the same bias). The plots show almost linear relation between the two gate biases: as V_P increases, V_B must decrease to balance it out, and in order to preserve same number of electrons. It can be seen from the figure that the gate bias needed for a

single electron is strongly dependent on the QD size. For smaller QDs, larger gate biases are required to maintain a single electron. This is analogous to a "particle in a box" problem, where the confined energy levels are inversely proportional to the confinement length. Therefore, for a smaller QD, it takes a larger gate bias to "push down" the energy states in order to align the ground state with the Fermi level.

To illustrate such relations, Fig. 3.8 compares the 1-D potential cut along X direction for two different bias sets. The blue curve is the potential resulting from one set of bias, V_{P1} and V_{B1}. If the barrier gate bias increases, thus lowering the barrier height, the plunger gate bias must decrease; raising the bottom of the potential well as well as the energy states in the QW, to make the ground state cross the Fermi level. The new potential profile is indicated as the green curve.

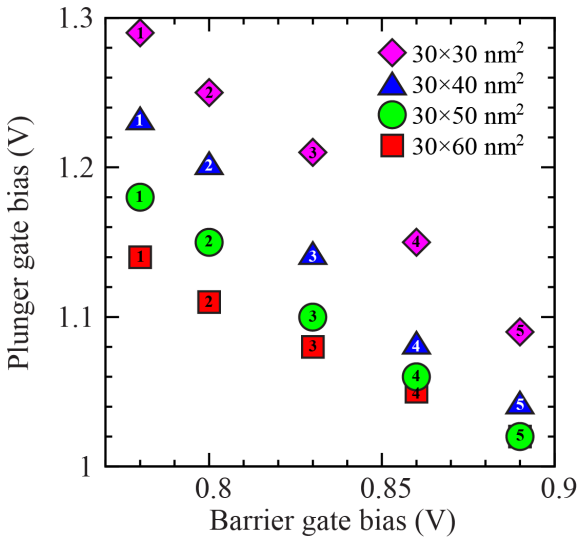

Fig. 3.7. V_B vs V_P when only single electron is present in the QD. Different dot color/shape represent different QD sizes. Simulations are grouped and labeled by numbers 1 to 5. Simulation runs with the same number have the same barrier gate bias.

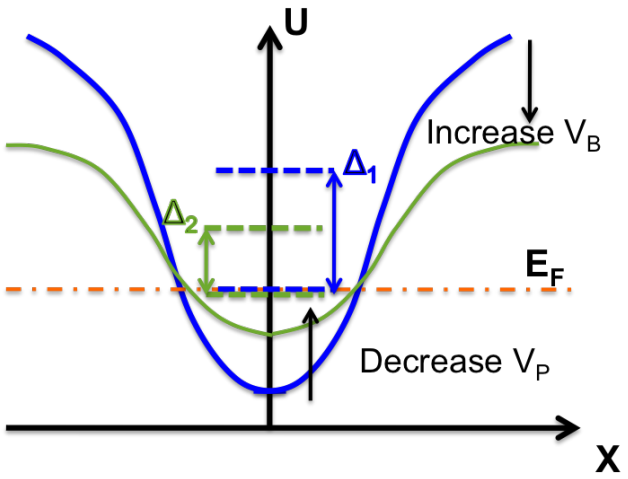

Fig. 3.8. Visualization of potential change along X direction. Initial potential profile is the blue curve, with VS of Δ_1 as the barrier gate potential V_B increases, the barrier is lowered, in order to align the ground energy state with the Fermi level to assure single electron, the gate bias V_P must decrease, thus raising the energy states, leading to the new potential shown as the green curve, with a smaller VS value Δ_2

3.4.3 Valley Splitting vs. Barrier Height, Electric Field

After each converged simulation, the VS is extracted as the difference between the lowest two eigenstates. In addition, the barrier height and the electric field at the oxide interface are also calculated. The barrier height is the energy difference between the top of the barrier and the Fermi level(which is fixed and assumed to be 1.1eV). The electric field is calculated from the converged potential profile from the relation: $E_{ox} = \frac{1}{q}\frac{\partial U}{\partial z}\,|_{z=0}$, where U is the potential profile and z is the direction perpendicular to the oxide interface. The VS is plotted against the E-field and barrier height and shown in Fig. 3.9(a) and 3.9(b) respectively. Different marker shapes in the figures represent different QD sizes.

Fig. 3.9(a) indicates that VS is almost linearly dependent on the E-field. As the E-field increases, the VS also increases. The QD size, on the other hand, does not

directly determine the VS, as can be seen from the figure. All shapes of dots almost align on the same line.

The barrier height dependence of VS can be seen in Fig. 3.9(b). The plot indicates that for a fixed QD size, the VS increases almost linearly as the barrier height. This is reasonable since higher barrier heights mean stronger confinement. On the other hand, if the barrier height is fixed, confinement inside smaller QDs is stronger, which in turn leads to larger VS.

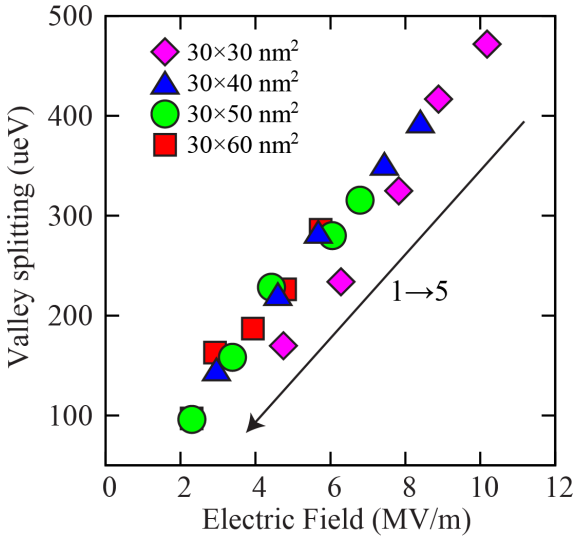

(a) Electric field dependence of VS for different QD sizes. VS is linearly proportional to the strength of the electric field at the oxide interface

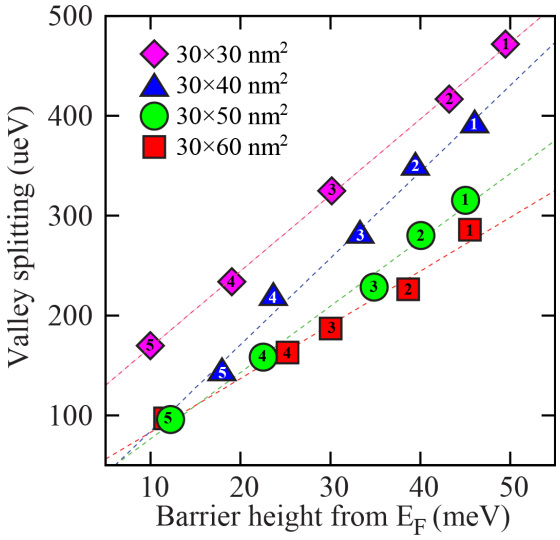

(b) Effect of the barrier height on VS for different QD sizes. As the barrier height reduces, confinement in the dot becomes weaker, and as a result VS decreases. On the other hand, if the barrier height is fixed, confinement inside smaller QDs is stronger, which leads to larger VS.

3.4.4 Valley Splitting Spectrum

Lastly, the VS for different QD sizes is plotted against V_B and V_P as a 2D color map, where the VS values in between samples are interpolated. This plot indicates the whole VS range that can be achieved, and ranges from 95 to 470 μeV. This is in good agreement with the experimentally measured value of $100\mu eV$ [40]. This plot can serve as a reference or look-up map to guide experimental designs of MOS QD devices with specific VS values.

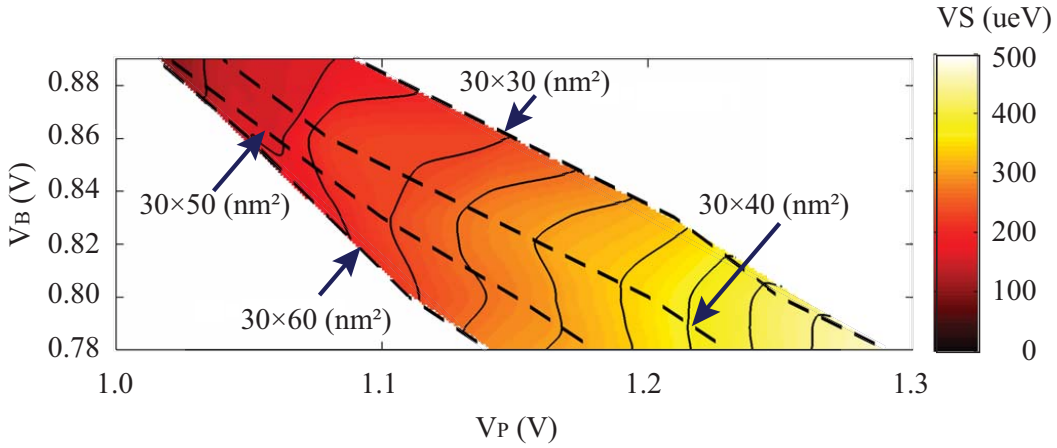

Fig. 3.9. Interpolated color map plot of VS distribution as a function of V_P and V_B in the single-electron regime. Dashed line indicates (V_P , V_B) for different QD sizes as indicated in the plot. V_P in the figure is the bias required to fill in a single electron with given V_B and size of the dot.

3.5 Conclusion

A Si MOS based quantum dot has been successfully modeled with NEMO3D-peta. The electronic structure of the Si substrate is represented by an atomistic $sp^3d^5s^*$ tight-binding Hamiltonian. NEMO3D-peta utilizes an efficient 3D spatial parallelization scheme that allows the self-consistent simulation of an 8-million-atom substrate within reasonable time limits. The range of VS has been calculated under various gate biases. Simulation results show that the VS of the MOS quantum dot

device in the single electron regime can be tuned by applying various gate biases. The calculated range of VS is comparable to known experimental results. The effects of gate size on VS as well as VS dependence on electric field and barrier height have also been explored and results showed trends consistent to experiments.

4. SUMMARY AND FUTURE WORK

Chapter 1 of this thesis addresses the device scaling challenge and how it impedes the trend of device performance enhancement which has continued for the past several decades. Computational modeling serves as an important tool in studying novel device concepts, and ultimately finding solutions to the scaling challenge. This thesis utilizes the computational modeling approach in studying two types of devices, graphene nanostructures and single-electron quantum dots. Chapter 2 and 3 addresses each one of these two subjects.

Chapter 2 begins with introducing the unique properties of graphene, such as its giant mobility, high electron velocity, and 2D nature, and how these properties are related to electronic devices. The biggest challenge in utilizing graphene in transistor applications has been the zero bandgap in graphene. Various graphene processing techniques and graphene based nanostructures have been proposed to engineer a bandgap in graphene. One of these examples is fabricating periodic perforation in graphene, making graphene nanomeshes (GNM). This work then focuses on modeling GNM using an advanced nearest neighbor tight-binding model, namely the p/d model. Details and advantages of the p/d model is discussed. Two types of hole geomotries, circular and rectangular holes, are studied in details. Simulation results confirm that a variable bandgap can be obtained by tuning the hole size. Further study also revealed interesting properties of GNM edges, which lead to anisotropic electronic properties along different directions in rectangular hole GNMs. It is concluded that the bandstructure of graphene can be engineered by various hole geometries, which makes GNM attractive for novel device applications. A complete understanding of hole geometry and edges effects can potentially lead to the capability of making a specific GNM structure that is tuned and customized for a specific task or device. However, in order to fully harness the potential of GNM, atomic precision lithography

is necessary in order to create a clean GNM structure with defined edges, since the electronic properties of GNM is sensitive to the exact hole and edge geometries.

To fully reveal the bandstructure engineering capabilities of GNM, more understanding needs to be gained on how the hole geometry and edge effects affect the bandstructure.Therefore, other hole geometries, such as triangular, hexagonal shaped holes in GNM need to be studied. Important quantities such as the bandgap needs to be summarized and tabulated under various conditions. In order to unveil the device capabilities of GNM, charge self-consistent transport simulation must be performed, with gates included and biase voltages applied. Important quantities of interest, such as on-off ratio, sub-threshold slope(SS) needs to be extracted from I-V curve and compare to current existing devices.

Reliablity test is an essential task before proposing GNM for novel device applications. In this work, GNM structures constructed for simulation study are same size, perfectly aligned, and with no defect on the edges. In reality, however, the fabrication process induces many non-idealities including hole size variation, mis-alignment, and edge roughness, all of which will play roles in influencing device performances. Further simulations that include these non-idealities must be carried out to determine how susceptible to non-idealities are the properties of GNM based devices.

Chapter 3 is focused on studying the valley splitting (VS) in a single electron quantum dot based on Si MOS structure. The importance of VS regarding quantum computing is discussed. Eigenstates of the quantum dot are calculated charge self-consistently and the VS are extracted under various biasing conditions. Simulation results indicate that the VS in this quantum dot can be controlled by tuning the potential barrier and gate geometry. Full range of the achievable VS is determined, which matches the VS range measured experimentally.

As for future work, a number of factors need to be investigated to predict the VS more accurately, such as Si/SiO_2 interface roughness and surface charge. To fully understand the electron tunneling events in the quantum dot and reproduce the experimental charge stability diagram, source and drain terminals need to be included

in the modeling domain. Potential profiles across the entire device, including source and drain, under various biasing conditions need to be described. The eigen-energy spectrums under two and multiple electron regime need to be calculated, which means electron-electron interaction must be correctly modeled inside the quantum dot.

LIST OF REFERENCES

LIST OF REFERENCES

[1] R. Schaller, *Moore's law: past, present and future* IEEE Spectrum, pp. 52-59, Jun 1997

[2] G. E. Moore, *Cramming More Components onto Integrated Circuits* Components, vol. 86, no. 1, pp. 82-85, 1998.

[3] S.E.Thompson and S.Parthasarathy, *Moore's law: the future of Si microelectronics* Materials Today, vol. 9, no. 6, June 2006.

[4] K. S. Novoselov, A. K. Geim, S. V. Morozov, D. Jiang, Y. Zhang, S. V. Dubonos, I. V. Grigorieva and A. A. Firsov, *Electric Field Effect in Atomically Thin Carbon Films* Science vol. 306 no. 5696 pp. 666-669

[5] S. Steiger, M. Povolotskyi, H.-H. Park, T. Kubis, and G. Klimeck, *NEMO5: A Parallel Multiscale Nanoelectronics Modeling Tool* IEEE Transactions on Nanotechnology 10, 1464 (2011)

[6] P.R.Wallace *The band theory of graphite* Phys. Rev. 71, 622-634 (1947).

[7] F.Schwierz, *Graphene transistors* Nature Nanotechnology 5, 487-496 (2010)

[8] Zhihong Chen, Yu-Ming Lin, Michael J. Rooks, Phaedon Avouris, *Graphene nano-ribbon electronics* Physica E: Low-dimensional Systems and Nanostructures, Volume 40, Issue 2, December 2007, Pages 228-232

[9] Yuanbo Zhang, Tsung-Ta Tang, Caglar Girit, Zhao Hao, Michael C. Martin, Alex Zettl, Michael F. Crommie, Y. Ron Shen and Feng Wang, *Direct observation of a widely tunable bandgap in bilayer graphene* Nature 459, 820-823 (11 June 2009)

[10] S. Y. Zhou, G. H. Gweon, A. V. Fedorov, P. N. First, W. A. de Heer, D. H. Lee, F. Guinea, A. H. Castro Neto and A. Lanzara *Substrate-induced bandgap opening in epitaxial graphene.* Nature Materials 6, 916 (2007)

[11] Vitor M. Pereira, A. H. Castro Neto and N. M. R. Peres, *Tight-binding approach to uniaxial strain in graphene* Phys. Rev. B 80, 045401 (2009)

[12] A. Geim, *A Graphene update* Bull. Am. Phys. Soc. 55, abstr. J21.0004, http://meetings.aps.org/link/BAPS.2010.MAR.J21.4 (2010).

[13] D.Frank, Y.Taur and H.P.Wong, *Generalized Scale Length for Two-Dimensional Effects in MOSFETs* IEEE Electron Device Letters, vol. 19, no. 10, October 1998

[14] Patrik Recher and Bjorn Trauzettel, *Viewpoint: A defect controls transport in graphene* Physics 4, 25 (2011)

[15] L.Yang, C.Park, Y.Son, M.Cohen and S. Louie *Quasiparticle Energies and Band Gaps in Graphene Nanoribbons* PRL 99, 186801 (2007)

[16] Han, M. et al. *Energy band-gap engineering of graphene nanoribbons* Phys. Rev. Lett. 98, 206805 (2007).

[17] M. Evaldsson, I. V. Zozoulenko, Hengyi Xu and T. Heinzel *Edge-disorder-induced Anderson localization and conduction gap in graphene nanoribbons* PHYSICAL REVIEW B 78, 161407 (2008)

[18] Jingwei Bai, Xing Zhong, Shan Jiang, Yu Huang and Xiangfeng Duan *Graphene Nanomesh* Nature Nanotechnology 5, 190 - 194 (2010)

[19] X.Liang, Y.S.Jung, S.Wu, A.Ismach, D.L.Olynick, S.Cabrini and J.Bokor *Formation of Bandgap and Subbands in Graphene Nanomeshes with Sub-10 nm Ribbon Width Fabricated via Nanoimprint Lithography* Nano Lett. 2010, 10, 2454-2460

[20] Timothy B. Boykin, Mathieu Luisier, Gerhard Klimeck, Xueping Jiang, Neerav Kharche et al. *Accurate six-band nearest-neighbor tight-binding model for the - bands of bulk graphene and graphene nanoribbons* J. Appl. Phys. 109, 104304 (2011)

[21] Supriyo Datta Quantum Transport: Atom to Transistor Cambridge Press (2005) ISBN 978-0-521-63145-7

[22] Mathieu Luisier, Andreas Schenk, Wolfgang Fichtner and Gerhard Klimeck *Atomistic simulation of nanowires in the $sp^3d^5s^*$ tight-binding formalism: From boundary conditions to strain calculations* PHYSICAL REVIEW B 74, 205323 (2006)

[23] W. Y. Kim and K. S. Kim, *Carbon nanotube, graphene, nanowire, and molecule-based electron and spin transport phenomena using the nonequilibrium Green's function method at the level of first principles theory* J. Comput. Chem., 29: 1073-1083. (2008)

[24] Y. W. Son, M. L. Cohen and S. G. Louie *Half-metallic graphene nanoribbons*Nature 444, 347-349 (16 November 2006)

[25] T. Zibold and P. Vogl *Theory of semiconductor quantum-wire-based single- and two-qubit gates* Phys. Rev. B 76. 195301 (2007)

[26] B.Kane, *A silicon-based nuclear spin quantum computer* Nature, vol. 393, p.133 (1998)

[27] A. Gusev and A. Bulanov, *High-purity silicon isotopes ^{28}Si,$^{29}Siand^{30}Si$* Inorganic Materials, vol. 44, pp. 1395-1408, 2008.

[28] L. C. L. Hollenberg, A. S. Dzurak, C. Wellard, A. R. Hamilton, D. J. Reilly, G. J. Milburn, and R. G. Clark, Charge-based quantum computing using single donors in semiconductors Phys. Rev. B 69, 113301 (2004)

[29] C. Tahan, M. Friesen, and R. Joynt, *Decoherence of electron spin qubits in Si-based quantum computers* Phys. Rev. B 66, 035314 (2002)

[30] B. Koiller, X. Hu, and S. Das Sarma, *Exchange in silicon-based quantum computer architecture* Phys. Rev. lett 88, 027903 (2001)

[31] A. L. Saraiva, M. J. Calderon, X. Hu, S. D. Sarma, and B. Koiller, *Intervalley coupling for silicon electronic spin qubits: Insights from an effective mass study* arXiv:1006.3338 (2010)

[32] T.B.Boykin, N.Kharche and G.Klimeck, *Valley splitting in finite barrier quantum wells* Phys. Rev. B 77, 245320 (2008)

[33] T.B. Boykin, G.Klimeck, M.A.Eriksson, M. Friesen and S.N. Coppersmith et al., *Valley splitting in strained silicon quantum wells* Appl. Phys. Lett. 84, 115(2004)

[34] R.Rahman, J.Verduijn, N.Kharche, G.P.Lansbergen, G.Klimeck, L.C.L. Hollenberg, and S.Rogge, *Engineered valley-orbit splittings in quantum-confined nanostructures in Silicon* Phys. Rev. B 83, 195323 (2011)

[35] Z.Jiang, N.Kharche, T.Boykin and G.Klimeck, *Effects of Interface Disorder on Valley Splitting in SiGe/Si/SiGe Quantum Wells* Applied Physics Letters Vol100 issue10 (2012); doi: 10.1063/1.3692174

[36] M. A. Wilde, M. Rhode, Ch. Heyn, D. Heitmann, and D. Grundler, *Direct measurements of the spin and valley splittings in the magnetization of a SiSiGe quantum well in tilted magnetic fields* Phys. Rev. B 72, 165429 (2005)

[37] K. Lai, T. M. Lu1, W. Pan, D. C. Tsui, S. Lyo1, J. Liu, Y. H. Xi, M. Muhlberger, and F. Schaffler *Valley splitting of $SiSi_{1x}Ge_x$ heterostructures in tilted magnetic fields* Phys. Rev. B 73, 161301(R) (2006)

[38] Srijit Goswami, K. A. Slinker, Mark Friesen, L. M. McGuire, J. L. Truitt, Charles Tahan, L. J. Klein1, J. O. Chu, P. M. Mooney, D. W. van der Weide, Robert Joynt, S. N. Coppersmith and Mark A. Eriksson *Controllable valley splitting in silicon quantum devices* Nature Physics 3, 41 - 45 (2007)

[39] M. Xiao, M. G. House, and H. W. Jiang *Parallel spin filling and energy spectroscopy in few-electron Si metal-on-semiconductor-based quantum dots* Appl. Phys. Lett. 97, 032103 (2010)

[40] W. H. Lim, C. H. Yang, F. A. Zwanenburg, A. S. Dzurak *Spin filling of valley-orbit states in a silicon quantum dot* arXiv:1103.2895v2

[41] W. H. Lim, F. A. Zwanenburg, H. Huebl, M. Mottonen, K. W. Chan1, A. Morello, and A. S. Dzurak *Observation of the single-electron regime in a highly tunable silicon quantum dot* Appl. Phys. Lett. 95, 242102 (2009)

[42] G. Klimeck, F. Oyafuso, T. B. Boykin, R. C. Bowen and P. von Allmen, *Development of a nanoelectronic 3-D (NEMO 3-D) simulator for multimillion atom simulations and its application to alloyed quantum dots* (INVITED), Computer Modeling in Engineering and Science (CMES) Vol. 3, No. 5, pp 601-642, 2002

[43] G. Klimeck, S. Ahmed, H. Bae, N. Kharche, R. Rahman, S. Clark, B. Haley, S. Lee, M. Naumov, H. Ryu, F. Saied, M. Prada, M. Korkusinski and T. B. Boykin, *Atomistic Simulation of Realistically Sized Nanodevices Using NEMO 3-D: Part I - Models and Benchmarks* (INVITED) Special Issue on Nanoelectronic Device Modeling in IEEE Transactions on Electron Devices, Vol. 54, Issue 9, Sept. 2007, pp 2079-2089 (2007), ibid pp 2090-2099

[44] Shaikh Ahmed, Neerav Kharche, Rajib Rahman, Muhammad Usman, Sunhee Lee, Hoon Ryu, Hansang Bae, Steve Clark, Benjamin Haley, Maxim Naumov, Faisal Saied, Marek Korkusinski, Rick Kennel, Michael McLennan, Timothy B. Boykin, Gerhard Klimeck, *Multimillion Atom Simulations with NEMO 3-D* arXiv:0901.1890v1 [physics.comp-ph]

[45] Neerav Kharche, Marta Prada, Timothy B. Boykin, and Gerhard Klimeck, *Valley splitting in strained silicon quantum wells modeled with* 2^o *miscuts, step disorder, and alloy disorder* Appl. Phys. Lett. 90, 092109 (2007)

[46] G. Lansbergen et al., *Gate-induced Quantum-connement Transition of a Single Dopant Atom in a Silicon FinFET* Nature Physics, vol 4, Aug. 2008.

[47] Sunhee Lee,Hoon Ryu,Huw Campbell,Lloyd C. L. Hollenberg,Michelle Y. Simmons,and Gerhard Klimeck, *Electronic structure of realistically extended atomistically resolved disordered Si:P (δ-doped layers* PHYSICAL REVIEW B 84, 205309 (2011)

[48] B. Weber,S. Mahapatra,H. Ryu,S. Lee,A. Fuhrer,T. C. G. Reusch,D. L. Thompson,W. C. T. Lee,G. Klimeck,L. C. L. Hollenberg and M. Y. Simmons, *Ohm's Law Survives to the Atomic Scale* Science 335, 64 (2012)

[49] Martin Fuechsle, Jill A. Miwa, Suddhasatta Mahapatra, Hoon Ryu, Sunhee Lee, Oliver Warschkow, Lloyd C. L. Hollenberg, Gerhard Klimeck, Michelle Y. Simmons, *A Single-Atom Transistor* Nature Nanotechnology 7, 242246 (2012)

[50] Sunhee Lee, *Development of a Massively Parallel Nanoelectronic Modeling Tool and Its Applications to Quantum Computing Devices* Sunhee Lee's PhD thesis, Purdue University (2011)

[51] R. Jabr, M. Hamad, and Y. Mohanna, *Newton-Raphson solution of Poisson's equation in a pn diode* International Journal of Electrical Engineering Education, vol. 44, no. 1, pp. 23-33, 2007

[52] *http://en.wikipedia.org/wiki/Graphene*

[53] *http://en.wikipedia.org/wiki/Drain_Induced_Barrier_Lowering*